

On the γ -ray / Sub-mm Connection in AGN

S. M. Ward

Level 4 Project MPhys Physics & Astronomy

Supervisors: Prof P. Chadwick & Dr A. Brown

Department of Physics, Durham University

Submitted: April 21, 2020

Blazars, radio-loud Active Galactic Nuclei (AGN) with highly relativistic and collimated jets aligned close to our line-of-sight, are unique astrophysical laboratories, that serve as a direct probe into some of the most extreme and high-energy environments in the known Universe. Given the jets' intimate connection with the central engine, and their role in stifling star formation over cosmic time, understanding blazar emission mechanisms, locations and key governing parameters that give rise to the blazar sub-classes, namely the Flat-Spectrum-Radio-Quasars (FSRQs) and BL Lacertae Objects (BL Lacs), is of central importance in modern astrophysics (§1). This study performs correlation analysis on 11-years (54767-58785 MJD) of weekly-binned *Fermi*-LAT gamma-ray (§2, §3) and irregularly sampled Sub-Millimeter Array radio (§4) light curves, in bands of 0.1-10 GeV and 1.1-1.4 mm respectively, of 12 bright and variable blazars selected from a variety of sub-classes, so as to elucidate and constrain the emission mechanisms and locations in blazars.

Results of Discrete-Cross-Correlation-Function (DCCF) analysis (§5) are largely inconclusive; poor radio sampling acutely limits their utility, inducing false positive correlation peaks ($>3\sigma$), and apparently damping those owing to the true underlying correlation. With confidence though, FSRQ 4C+38.41 exhibits a $>8.38\sigma$ correlated peak, with a gamma-ray leading lag 23 ± 13 d, consistent with the shock-in-jet scenario in a static single-zone model. BL Lac S5 0716+71 exhibits a similarly significant radio-leading (-20 ± 6 d) anti-correlation over a limited time-series ($t < 56800$ MJD), which is not readily accounted for by theoretical models. Encompassing all correlations, gamma-ray and radio leading lags in FSRQs and Low-Synchrotron-Peaked BL Lacs, respectively, evidence loose consistency with the model of radiative cooling. Fixed energy range observations may account for the causal disconnect in higher-peaked BL Lacs; alternatively, inclination may be a key governing parameter, assuming an emission mechanism that does not dominate the entire jet cross section e.g. spine-sheath, needle-in-jet scenario. Lack of global correlation in outliers 3C 279 (FSRQ) and BL Lacertae demonstrates long ($>$ year) and short (\lesssim month) time-scale coupling are independent traits, implying multiple discrete mechanisms may act in all blazars, regardless of sub-class. Future correlation analysis must examine well-sampled regions on shorter time-scales over a blazar-specific energy range, and evaluate lag dependence on spectral/flux state. Supported by a suite of gamma-ray and radio observatories, studies of new VHE ($>$ TeV) blazars with the upcoming Cherenkov Telescope Array will directly test and constrain our current theoretical models of blazar emission.

CONTENTS

1	Introduction	3
1.1	Blazar Population Studies	4
1.2	Emission Locations & Correlation Studies	6
2	<i>Fermi</i> -LAT Data	7
2.1	Data Acquisition	7
2.2	Data Resolution	9
2.3	Catalogs & Target Selection	10
3	γ -ray Light Curves	11
3.1	Data Cuts	11
3.2	Analysis Pipeline	13
3.3	Residual Map Solutions	15
4	Sub-Millimeter Array Data & Radio Light Curves	16
4.1	Data Acquisition	17
4.2	Data Resolution & Light Curve Construction	18
5	Correlation Analysis	18
5.1	DCCF & Lag Measurement Prescription	19
5.2	Confidence Tests & Results	21
5.3	Split-Band Analysis	24
6	Discussion	25
7	Conclusions	28
	Acknowledgments	29
	References	29
A	Gamma-Ray Core Location	32
B	<i>Fermi</i> -LAT Backsplash Effect, Readout & Event Processing	32
C	Residual Map Solutions	33
D	SMA Array Design	34
E	Success Rate Prescription	35
F	Target Notes	35
G	Tables & Figures	40

1. INTRODUCTION

Highly luminous Active Galactic Nuclei (AGN) are powered by the conversion of potential to kinetic/electromagnetic energy during gas accretion onto a central super-massive black hole (SMBH, mass $M \sim 10^6\text{-}10^{10} M_\odot$) [1], and are widely studied as probes of accretion physics, strong-regime general relativity, and galaxy evolution models [2, 3]. Found in $\sim 1\%$ of all known galaxies [4, 5], roughly $\sim 10\%$ of AGN are defined as being ‘radio-loud’, implying a radio to optical flux density ratio, $R \geq 10$ [6, 7]. A pair of highly relativistic and collimated plasma jets emanate from radio-loud AGN, which emit over the entire electromagnetic spectrum, and spatially extend over 12 orders of magnitude, from AU - Mpc scales [8–10]. To date, there are 3138 *Fermi*-catalogued ‘blazars’ (§ 2.3) [11], that comprise the subset of all known AGN with jets directed close to our line-of-sight [8].

Owing to relativistic beaming or ‘Doppler boosting’, blazar jet emission dominates the entire AGN spectrum [12], making them ideal targets for jet studies. Exhibiting ‘superluminal’ motion [13], high optical polarisation [7, 10, 14], rapid flux variations on <minute timescales, long-term variability over >year timescales [15, 16], and both ‘redder’ and ‘bluer-when-brighter’ spectral variability [17, 18], blazars are fascinating targets of study. Moreover, understanding the underlying physics of jet formation/emission is of central importance in modern astrophysics, not least because the jets are intimately connected with the central BH engine, through BH spin and/or accretion processes¹(§1.1) [9, 12], but because AGN feedback plays a pivotal role in stifling star formation in galaxy clusters [22, 23]. Understanding the jet energy budget, energy transfer mechanisms and the associated efficiency are all key; in turn, this requires constraints on emission models, and the jet plasma constituents (§1.1, 1.2) [23, 24].

More generally, the intrinsic parameters that govern and motivate the blazar sub-classification scheme (§1.1) are not well understood. Key parameters could be any of: BH mass/spin, accretion rate/efficiency, galaxy type, inclination etc. [25]. By comparing and contrasting spectral energy distributions of various blazar sub-classes, §1.1 demonstrates that both accretion rate and BH mass likely have a bearing on blazar sub-classification. Our investigation, instead, evaluates the results of correlation analysis, and examines the dependency, if any, on BH mass.

Correlation analysis is performed on gamma-ray and radio light curves of 12 blazars, spanning ~ 11 years of *Fermi*-LAT (§2) and Sub-Millimeter Array (§4) data, with the aim of elucidating and constraining the high-energy emission mechanisms and locations in blazars. §1.1 describes our understanding to date of the blazar population, thereby addressing the likely origin of the low-energy seed photons for high-energy emission. In §1.2, observational traits of jet emission models are briefly detailed, and a review of radio/gamma-ray correlation studies is conducted. Following this, §2 and §3 describe how gamma-ray data is acquired and processed for gamma-ray light curve construction. Similarly, §4 details radio light curve construction. Correlation analysis is performed in §5, with results discussed, and leads for future work detailed in §6, before drawing overarching conclusions in §7.

¹ In the Blandford-Znajek mechanism, the jet bulk energy is governed by the black hole spin, whereby magnetic-spin extraction of BH rotational energy leads to collimated jets that propagate along the BH spin axis [19, 20]. Conversely, the Blandford-Payne mechanism describes jet formation through accretion processes, with the jet axis instead aligned with the disk plane normal [21].

1.1. Blazar Population Studies

The emission mechanisms in blazars have been constrained by analysing broadband spectral energy distributions (SEDs). Blazars unanimously share a characteristic, double-peaked, broadband SED, dominated by non-thermal emission (e.g. Fig. 1), that can span from sub-GHz ($>$ metre) radio frequencies (wavelengths) through to $>$ TeV gamma-ray energies, with humps peaking in the Infrared - X-ray and MeV - TeV gamma-ray bands respectively [7, 10]. The accepted paradigm is that the low energy component is dominated by synchrotron emission, originating from a non-thermal population of highly relativistic electrons (and/or positrons), accelerating in some local magnetic field (see e.g. pp.739 Ref. [26] for a recent review). The origin of the high energy component is, however, less well understood.

Most often, ‘leptonic scenarios’ are cited to account for the high energy component, whereby the Inverse Compton (IC) process up-scatters low energy seed photons via interactions with the population of relativistic electrons/positrons (responsible for synchrotron emission, e.g. [10]). However, protons in ‘hadronic scenarios’ may be responsible for up-scattering [27, 28]. Moreover, low-energy seed photon sources are not yet clearly identified [28]. Seeds are likely a mix of the synchrotron photons themselves (Self-Synchrotron Compton, SSC) [29], and photons from external sources (External Radiation Compton, ERC), i.e. those originating from the accretion disk [30, 31], the broad line region (BLR) [32], and/or the dusty molecular torus [33].

Such variations in emission pathways/mechanisms likely account for the observational characteristics exhibited by the blazar sub-classes, denoted ‘Flat-Spectrum-Radio-Quasars’ (FSRQs²) and ‘BL Lacertae Objects’ (BL Lacs³). By convention, the presence/width of optical lines is the distinguishing feature, with FSRQs exhibiting strong/broad emission lines, and BL Lacs exhibiting weak/narrow or no emission lines. As proposed by Urry & Padovani (1995) [8], a rest-frame line equivalent width, $EW = 5\text{\AA}$, marks the boundary between these blazar sub-classes. BL Lacs are further divided into classes of high, intermediate and low synchrotron frequency peak (HBL, IBL, LBL respectively [34], more in Table. II).

Luminosity-binned average SEDs were constructed to investigate these optical discrepancies (Fig. 1) [35, 36]. The resulting ‘blazar sequences’ are controversial due to the limited sensitivity of gamma-ray observations (by the ‘Energetic Gamma-ray Experiment Telescope’ (EGRET), and the 20 times more sensitive *Fermi*-LAT), that impose selection biases. However, the results are readily accounted for through the model of ‘radiative cooling’, under the assumption that the highest black hole mass blazars have (inadvertently) been selected (§6). Normalising the disk luminosity, L_D , to the Eddington luminosity, L_{Edd} , a disk ratio, $\lambda_D = \frac{L_D}{L_{Edd}}$, is defined⁴.

Authors conclude the FSRQs have a radiatively efficient accretion disk ($\lambda_D > 0.01$), producing an excess of low-energy seed photons through direct transmission onto the jet plasma, and via reflection off of the BLR clouds and the torus. Thus, FSRQs are likely a mix of SSC and ERC, where the latter dominates. BL Lacs, however, have a radiatively inefficient disk

² ‘Flat’-term originates from FSRQ radio spectral index, often, $\alpha \lesssim 0.5$, with flux density, $S_\nu \propto \nu^{-\alpha}$ [26].

³ BL Lacertae, perhaps the first blazar to be discovered (1929), is the ‘prototype’ of all BL Lacs [26].

⁴ Observational findings motivate a revised classification scheme of the blazar sub-classes, with a boundary marked instead by $\lambda_D = 0.01$ [12, 35]. Given BL Lacs can, in fact, temporarily exhibit lines, $EW > 5\text{\AA}$, this scheme is particularly desirable. However, difficulty in measuring BH mass, M_{BH} , has delayed this revision (where $L_{Edd} \propto M_{BH}$).

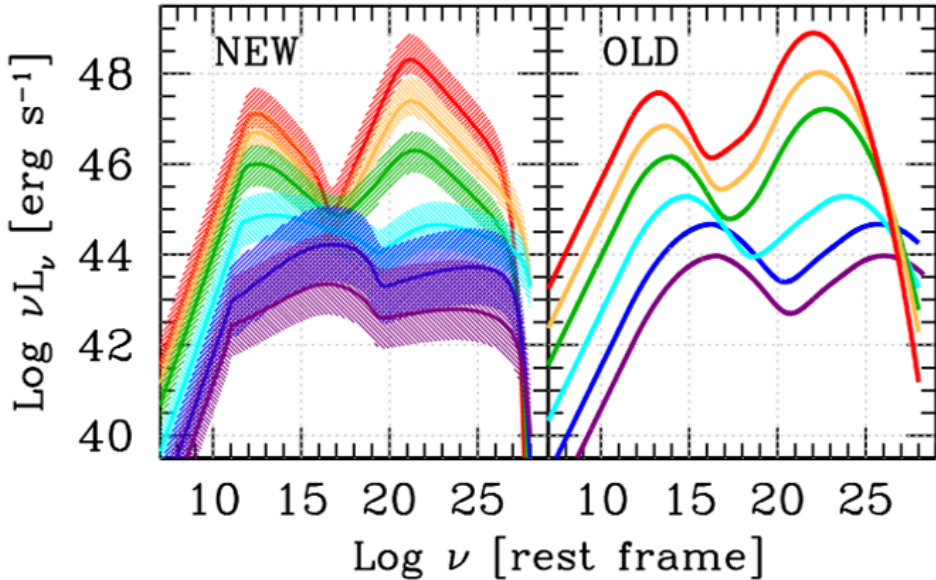


FIG. 1: Empirical plot from Ghisellini et al. (2017) [35], compares ‘Blazar Sequences’ of luminosity-binned average SEDs from 2017 (*Left*) and 1998 (*Right*). *Left*: ‘Blazar Sequence 2’ employs multi-wavelength data sets (radio, optical, X-ray, gamma-ray) of 745 blazars [7, 35], binned according to gamma-ray luminosity. While BL Lacs conform to the original blazar sequence (right panel), FSRQ SED peak frequencies are independent of luminosity bin. *Right*: Original ‘Blazar Sequence’ from Fossati et al. (1998) [36], employs radio and X-ray data sets from 126 blazars (of which only 33 were detected by EGRET), binned according to radio luminosity. As the luminosity decreases, the SED peaks shift to higher frequencies. Due to selection effects, FSRQs [red] appear to be more luminous and ‘redder’ than BL Lacs [blue]. These findings motivate the model of ‘radiative cooling’.

($\lambda_D < 0.01$), such that external seed photons are scarce, and SSC dominates (intuitively then, we might expect SSC-dominated BL Lacs to exhibit radio-leading lags). According to the model of radiative cooling, more seed photons incident on the jet plasma means more jet energy is lost to up-scattering, leading to a more red-shifted spectrum (Fig. 1). The width of the transition region across $\lambda_D = 0.01$ is poorly understood [35], and likely contributes towards the diversity in blazars SEDs. Refs. [7, 35, 36] detail ‘Compton dominance’, lower mass blazars, and the requirement that FSRQ magnetic field decreases with increasing luminosity.

The ‘simplified blazar scenario’ in Giommi et al. (2012) [104] provides an alternative to the ‘radiative cooling’ model, proposing that there is no link between blazar luminosity and SED, but as yet, there is no explanation for the underlying assumptions on which the model is based [7]. While the two competing models are, to date, consistent with observations (due to the selection effects imposed by *Fermi*-LAT), the discovery of some low-luminosity, ‘red’ BL Lacertae object would motivate a revision of the ‘radiative cooling’ model.

1.2. Emission Locations & Correlation Studies

The location of high-energy dissipation/emission (hereafter, ‘gamma-ray core’) is actively sought and widely debated, as it indicates the origin of low energy seed photons for IC. Disk/BLR-ERC should dominate for an emission site located at sub-pc scales from the black hole, whereas torus-ERC/SSC should dominate on \gtrsim pc scales [28, 37–41]⁵. Independent evidence is lent both to a core residing ‘close’ to the black hole, within the BLR on sub-pc scales, *and* a distant gamma-ray core, located at $>$ pc scales. Appendix A details these observational findings. This section instead focusses on recent radio/gamma-ray correlation studies, and how their results can be interpreted, to constrain emission mechanisms/locations.

The ‘shock-in-jet scenario’, whereby synchrotron emission is produced as relativistic plasma propagates down the jet [44, 45], has earned credibility through various radio campaigns (see Ref. [46] for review of Very Long Baseline Interferometry (VLBI) jet studies). In particular, Ref. [37] observe a time-lag inversely proportional to radio frequency, $\tau \propto \nu^{-1}$, implying jet opacity is dominated by Synchrotron-Self-Absorption (SSA). As the shock front propagates downstream, it expands, thereby lowering the SSA cut-off frequency (or equivalently, the ν -dependent optical depth, τ_ν). Thus, flux peaks at increasingly lower frequencies. This is the ‘core-shift’, whereby the $\tau_\nu = 1$ ‘core’ resides at some ν -dependent distance from the SMBH.

On quantifying significant gamma-ray/radio time lags, τ , the high-energy emission is associated with these shock fronts, and $\sim c\tau$ is interpreted as a spatial offset of ‘cores’, i.e.,

$$\Delta r_{r,\gamma} = \frac{\beta_{app} c \tau}{\sin \theta (1 + z)}, \quad (1)$$

with observer frame properties: β_{app} , the shock front apparent velocity, θ , the line-of-sight/propagation-axis angle, and z , the redshift [37]. Almost exclusively, significant lags ($>3\sigma$) are gamma-ray leading, implying a gamma-ray core residing upstream of the radio core. Table I summarises results of recent radio/gamma-ray correlation studies. With multi-wavelength radio data, VLBI proper motions, and the assumption of a conical jet geometry, the jet-base/radio-core separation can be determined. Further, assuming the base separation from the SMBH is negligible, the distance to the gamma-ray core is determined [37]. This can then be contrasted with BLR location, calculated as in e.g. Ref. [47], to constrain seed photon source. However, limited to two radio bands (§4), our analysis is focussed solely on computing $\Delta r_{r,\gamma}$, and examining the correlation dependencies, if any, on blazar sub-class, and black hole mass.

Complex alternatives to the single-zone model are abundant e.g. needle-in-jet scenario [48], spine-sheath scenario [49], multi-zone discontinuous models [50, 51] etc. For our purposes, we note simply that a multitude of single zone cores could manifest in results of correlation analysis as multiple significant lags. Mixed lags could also be observed if the cores shift over time (this holds true for a single-zone model also). There is ample opportunity then, to test the static single-zone model over an 11-year time-series.

⁵ X-ray coronal emission driving disk reflections is often associated with the base of the jet (e.g. the ‘lamppost geometry’). Thus, constraints on the location of the high-energy emission source (as a function of time) can further our understanding of the central engine as a whole [42]. Similarly, variability time-scales indicate source compactness [43].

TABLE I: Results of previous radio/gamma-ray correlation analyses are displayed. Columns show radio frequency of observations, ν_{radio} , light curve (LC) length, t_{obs} , gamma-ray time-binning (weekly: ‘W’, and monthly: ‘M’), and the number of significant ($>3\sigma$) correlations, $N_{significant}$, decomposed into those owing to FSRQS, N_{FSRQs} , and BL Lacs, $N_{BL\ Lacs}$. These are further decomposed into lags that are gamma-ray leading, (+’), lagging, (-’), and those consistent with $\tau = 0$, (‘0’). All *Fermi*-LAT gamma-ray LCs are constructed over the energy range 0.1-200 GeV (except Ref. [37]: 0.1-300 GeV). Ref. [39] analyse weekly and monthly binned gamma-ray LCs; only lags significant in both analyses are included (thereby excluding 3 targets). Every lag is of the order ~ 10 -100 d, with no measurements in excess of 1000 d; typical core separations are of the order ~ 0.1 -10 pc. Gamma-ray leading lags, consistent with the shock-in-jet scenario, dominate, featuring in 19 out of 22 cases, with only 1 target exhibiting a radio-leading lag. False positive measurements are explored in §5.2.

Reference	ν_{Radio} / GHz	t_{obs} / year	Binning	$N_{significant}$	$N_{FSRQs}(+, -, 0)$	$N_{BL\ Lacs}(+, -, 0)$
[38]	15	4	W	1 / 41	(0,0,0)	(1,0,0)
[28]	15	8	M	2 / 145	(0,0,0)	(2,0,0)
[39]	37	5	W/M	4 / 55	(2,1,0)	(1,0,0)
[40]	37	2.5	W	2 / 15	(2,0,0)	(0,0,0)
[37]	86	3.5	M	9 / 54	(5,0,1)	(2,0,1)
[40]	95	2.5	W	4 / 15	(3,0,0)	(1,0,0)

2. *FERMI*-LAT DATA

The *Fermi* Gamma-Ray Space Telescope (*Fermi*), launched on 11th June 2008, carries two gamma-ray sensitive instruments, that observe the cosmos in the range 10 keV - 300 GeV. The Large Area Telescope (LAT), with minimum energy range 20 MeV - 300 GeV, is the primary instrument on-board *Fermi*, which is supplemented in studies of gamma-ray bursts by the Gamma-Ray Burst Monitor (GBM)⁶. This study employs LAT data only, of 12 blazars (Tables. II, III), over ~ 11 years. §2.1 & 2.2 describe how raw *Fermi*-LAT data is acquired and processed for public use, with the target selection procedure laid out in §2.3. Information is primarily sourced from the ‘Fermi tools:Cicerone’ documentation⁷.

2.1. Data Acquisition

Fermi-LAT processes for observing astrophysical gamma-rays, and removing undesirable background interactions, are detailed here. LAT observations see the production of an electron-positron pair by an incident gamma-ray, occurring within one of the 16 tracker modules (TKRs). Each column-like TKR contains a set of 16 (high-Z) tungsten conversion foil plates, interleaved with 18 silicon XY tracker planes. Pair production, necessarily in the vicinity of an atomic nucleus [54], occurs in the tungsten plates, and passage of the resulting e^+e^- pair is recorded by the tracker planes⁸. Detectable pulses of charge induced in the Silicon Strip Detector (SSD)

⁶ The GBM provides low energy resolution, a full sky field of view, and $\sim 10\ \mu s$ temporal precision.

⁷ <https://fermi.gsfc.nasa.gov/ssc/data/analysis/documentation/Cicerone/>

⁸ A tracker plane is comprised of an array of Silicon Strip Detectors (SSDs), whereby each SSD holds x2 strips (one each for of (\hat{x}, \hat{y}) directions).

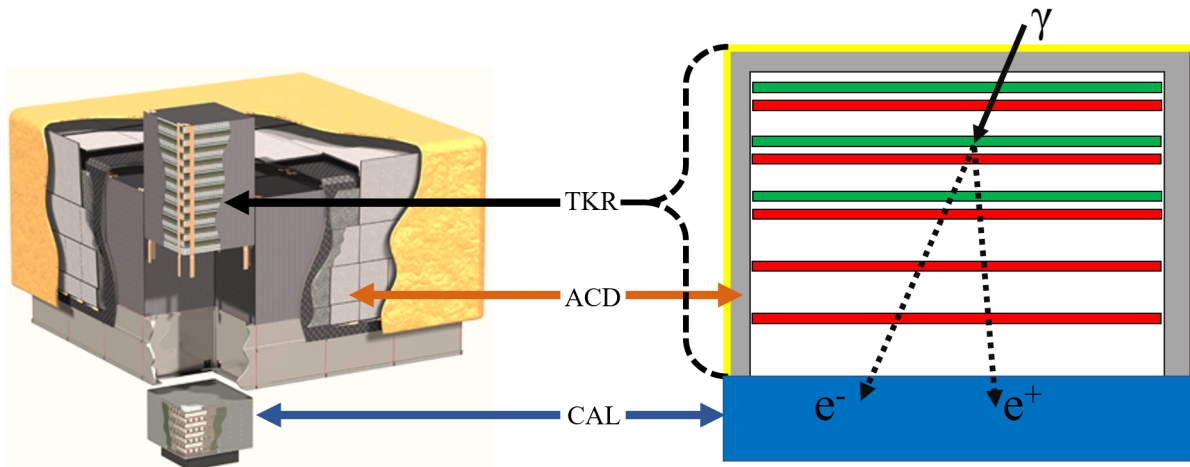


FIG. 2: *Left:* *Fermi*-LAT Schematic displays the TKR and CAL modules, and the segmented ACD [52]. *Right:* TKR representation shows an incident γ -ray transiting through the ACD [grey], producing an e^+e^- pair in a conversion foil [green], which subsequently transits through the tracker planes [red] for energy deposition in the CAL [blue]. Conversion foils are placed *above* the tracker planes (true LAT TKRs bear x16 and x18 respectively). The TKR trigger primitive, required for the global trigger that leads to event readout, is issued under a ‘3-in-a-row’ philosophy, requiring that SSD array signals (above a certain amplitude threshold) are issued in three consecutive tracker planes. Thus, only 16 conversion plates are included. The micrometeoroid shield/thermal blanket [yellow] protects the *Fermi*-LAT equipment; more details in Ref. [53].

array by transiting e^+e^- are readout via aluminium readout strips, providing XY plane localisation; combined with tracker plane height, particle trajectory is reconstructed [55, 56].

Incident photon energy, E_γ , is inferred through energy measurements made in the Calorimeter modules (x16 CALs), each comprised of 96 Caesium Iodide (CsI) scintillating crystals, located at the foot of TKRs. Scintillation light is read out by dual PIN photodiodes, measuring energy deposited by the EM shower induced by the e^+e^- pair in the CAL. Not all gamma-ray energy is deposited in the CALs; low energy photons (~ 100 MeV) deposit $\sim 50\%$ of their energy in the XY tracker planes, which is estimated from the number of interactions in the SSD arrays [55]. Fig. 2 showcases *Fermi*-LAT structure and highlights the pair production process.

Cosmic Rays (CRs), highly relativistic charged particles with energies overlapping and exceeding the LAT range [57, 58], can register in the LAT as an ‘event’⁹. CRs, in addition to noise contributions from e.g. Galactic diffuse emission, isotropic diffuse emission, Earth albedo gamma-rays etc.¹⁰, lead to an overwhelming background flux, with noise events exceeding those of true source gamma-rays by a factor $10^2\text{-}10^5$. The Anti-Coincidence Detector (ACD) is the first line of defence in combatting CR flux, designed to detect 99.97% of incident, singly charged particles [55]. This shield, which envelopes the LAT (Fig. 2), is comprised of 89

⁹ An ‘event’ is the LAT response to any type of interaction, regardless of whether the incident particle is an astrophysical gamma-ray, or background noise.

¹⁰ Earth albedo gamma-rays are products of CR interactions with the Earth's atmosphere (pp. 33 Ref. [56]).

segmented plastic scintillator tiles, that excite on CR interactions. Wavelength shifting fibres, coupled to 2 photomultiplier tubes, collect the scintillation light, which ultimately issues a ‘veto signal’, thereby flagging the data. ACD segmentation ensures the ‘backsplash effect’, whereby secondary event products induce additional veto-signals, is minimised (Appendix. B).

Details on the subsequent readout processes/conditions, on-board processing, and ground transmission/processing/filtering are described in full in Appendix. B. Most importantly, the on-board processing is performed by the Data Acquisition System (DAQ), operating under Pass 8 software, which maximises the acceptance of true source gamma-rays, while minimising the acceptance of CR interactions and other background events [55]. Combined, the on-board triggering system, filtering and ‘Level 1’ ground processing reduces the background rate by a factor 10^6 , while retention of true source gamma-ray events is $\sim 75\%$ [55]. Data is stored in the publicly accessible ‘photon files’ (*PH0*.fits).

2.2. Data Resolution

Following the event filtering procedures (§2.1), the retained gamma-rays, termed ‘counts’, must be deconvolved, by removing the imprints of the *Fermi*-LAT on the true incident spectrum (as in §3.2, 3.3). This section details the finite resolution of the *Fermi*-LAT, characterised by the instrument response function (IRF), which encompasses the angular resolution, energy resolution, and the effective collecting area. IRFs are constructed from Monte Carlo simulations, and as such are continually improved and updated (currently P8R3_V2).

For an incident gamma-ray with energy and direction of incidence (E_γ, \hat{p}), the probability of measuring \hat{p}' is described by the Point Spread Function (PSF), a function of ($E_\gamma, \hat{p}, \hat{p}', \text{evtype}$) [see evtype below]. Tracker plates are secured directly underneath conversion plates, ensuring e^+e^- are tracked immediately after conversion, thereby optimising the PSF [55]. However, scattering of e^+e^- particles within the TKR acts to reduce the angular resolution of the LAT. Further, emission of Bremsstrahlung radiation, a product of the e^+e^- particles decelerating as they transit down the TKR, leads to a larger PSF. Products of higher energy photons experience less scattering, and are thus better resolved. In addition, tungsten plate thickness changes with depth within the TKR, meaning angular resolution depends on the height of conversion. Pair production in one of the first 12 ‘thin’ plates (0.035 radiation lengths) of tungsten is recorded as a FRONT event type (evtype = 1), whereas conversion in one of the 4 remaining ‘thick’ plates (0.18 radiation lengths) is recorded as a BACK event type (evtype = 2)^{11, 12}. Pairs produced in BACK events experience more scattering, resulting in poorer angular resolution, and vice versa. Angular resolution improves from $\sim 3.5^\circ$ at 100 MeV to an upper limit $\sim 0.15^\circ$ at > 10 GeV (trends showcased in Ref. [56]). Selecting both FRONT and BACK events (evtype = 3) ultimately yields an unbiased sample of low and high energy gamma-rays.

‘Energy dispersion’ describes the probability distribution of measuring E'_γ , for an incident

¹¹ Multiple plate thicknesses ensures a high conversion probability (thick plates), while retaining good angular resolution (thin plates). Interaction probabilities for FRONT/BACK events are equal [56].

¹² Surplus to FRONT/BACK, event types divide data according to quality of PSF (evtype = 4, 8, 16, 32), and energy resolution (evtype = 64, 128, 256, 512) [increasing from worst to best quartiles]. IRFs do not permit evtype mixing.

photon of energy E_γ (LAT energy resolution $\lesssim 10\%$, more in §3.3, Appendix. C). Energy dispersion is a function of $(E_\gamma, E'_\gamma, \hat{p}, \text{evtype})$. Finally, the effective collecting area of the *Fermi*-LAT ($\sim 0.8 \text{ m}^2$), which depends on $(E_\gamma, \hat{p}, \text{evtype})$, is determined by the product of geometrical collecting area with the conversion probability and event type efficiency [56].

Once resolution has been characterised, photon event class (`evclass`) is assigned, where each is suited for different types of analysis. Classification is based on various criteria, including PSF, effective area, background contamination, reconstruction quality and photon conversion probability. Counts are classified by trialling the data with the most strict, ‘cleanest’, classification criteria, and then loosening the selection criteria until the event satisfies the required conditions. The cleanest event classes are ULTRACLEANVETO and SOURCEVETO, followed by ULTRACLEAN, CLEAN, SOURCE and TRANSIENT. Where the cleanest events have a low PSF and background contamination, there is a tradeoff of low effective area. Conversely, the TRANSIENT classes permit broad PSFs and high background fluxes (\geq Isotropic Diffuse Gamma-ray Background (IGRB) flux), but have the largest effective area. The SOURCE class (`evclass = 128`), striking a balance between low background flux (\leq IGRB flux) and PSF, with moderate effective area, is best suited for blazars off the Galactic plane ($|b| > 10^\circ$).

2.3. Catalogs & Target Selection

The *Fermi* 4FGL catalog, constructed from the first 8 years of *Fermi*-LAT observations, contains data on 5065 gamma-ray bright ($> 4\sigma$) sources (compared to its 3FGL predecessor containing 3033 sources), over an energy range 50 MeV - 1 TeV (extended from 100 MeV - 300 GeV) including name, position, flux, significance, variability, and best fitting spectral model [11]. In addition to 694 FSRQs, 1132 BL Lacs, and 1312 unclassified blazars (BCUs), 4FGL includes data on pulsars, supernova remnants (SNRs), pulsar wind nebular (PWNe), radio galaxies etc. Coupled with 4FGL, improved models that describe Galactic (`gll_iem_v07.fits`) and extra-galactic (`iso_P8R3_SOURCE_V2_v1.txt`) diffuse gamma-ray emission should be employed, as well as the most recent Pass 8 IRFs for SOURCE class events (`P8R3_SOURCE_V2`).

Ideal targets for light curve (LC) construction and correlation analysis are bright and variable blazars situated above/below the Galactic plane; these targets maximise the probability of yielding high activity LCs, and reduce data point uncertainty by maximising signal-to-noise ratio (SNR). The chi-squared distributed ‘Test Statistic’ (TS) is used as a proxy for source brightness, and is defined as twice the natural-log likelihood difference between models with and without the target [60–63]; \mathcal{L} is the maximum likelihood that the model fits the data. \mathcal{L}_1 (\mathcal{L}_0) models apply a best-fitting (zero) target normalisation (i.e. the null hypothesis). Thus,

$$TS = 2\ln\left(\frac{\mathcal{L}_1}{\mathcal{L}_0}\right). \quad (2)$$

The 4FGL ‘Variability_Index’, hereafter V_{4FGL} , is used to select the most variable blazars. Defined fully in pp.28-29 Ref. [11], it is written as a sum over log likelihoods fitted in each (1-year) time *interval*, as compared with the *full* (8-year) time-set; similarly, ‘Variability2

‘Index’, hereafter V_2 , is summed over 2-month intervals:

$$V_{4\text{FGL}} = \sum_{\text{intervals}} \log\left(\frac{\mathcal{L}_{\text{interval}}}{\mathcal{L}_{\text{full}}}\right) ; V = \frac{(F_{\max} - \sigma_{\max}) - (F_{\min} + \sigma_{\min})}{(F_{\max} - \sigma_{\max}) + (F_{\min} + \sigma_{\min})} \quad (3)$$

For clarity, the standard light curve variability index, hereafter V , is quoted above, which depends on maximum and minimum flux values, F , and their associated uncertainties, σ [64].

A list of blazar preferences from the 4FGL catalogue was created according to the procedures described below, yielding 6 FSRQs and BL Lacs each (totalling 12 preferred sources, Table. II, III). The even split of FSRQs and BL Lacs is desirable for investigating correlation dependencies, if any, on blazar subclass. For the same reason, an even split of LBLs, IBLs and HBLs is sought. By selecting only the brightest blazars, it is important to note our blazars likely follow the classical blazar sequence (Fig. 1, more in Fig. 3, §6).

All 5065 sources are loaded in via the 4FGL catalog; `gll_psc_v20.fit`. All sources other than FSRQs/BL Lacs are removed, and the 100 ‘brightest sources’ (according to TS) are extracted. Three constraints are then applied: $|b| > 10^\circ$ ensures sources are off the galactic plane, minimising galactic diffuse background emission. A variable source is defined with 99% confidence as having $V_{4\text{FGL}} > 18.48$; by examination of our list, this is excessively low, and we apply an arbitrary filter, $V_{4\text{FGL}} > 10^3$ to trim the list down. The third filter is $V_2 > 72.44$, which ensures there is a $< 1\%$ probability that the source is steady (over 8-years) [11]. A further constraint limiting the selection to the 30 brightest sources is then applied. Cross-referencing this list with the availability of SMA (§4, Table. III) and BH mass (Table. II) data, and appending the HBL Mrk 501 ($V_{4\text{FGL}}=293$), yields the final 12 source list, which is detailed in Table. II, III.

3. γ -RAY LIGHT CURVES

Fermi-LAT data are used to construct 12 ~ 11 -year weekly-binned gamma-ray light curves (LCs), from MET 246823875 - 594057870s \equiv 54767 - 58785 MJD \equiv 27/10/2008 - 29/10/19, in the range 0.1-10 GeV, and an additional 30 ‘split-band’ LCs in energy ranges spanning 1 order of magnitude. The Fermi Science Tools v1.2.1 (hereafter `Fermi tools`¹³) are employed for LC construction, which are implemented and readily utilised in Python with the `fermipy v0.17.4`¹⁴ Python package. `Fermi tools` are employed to de-convolve the astrophysical gamma-ray data with the IRF (§3.2), thereby creating a virtual ‘true’ sky emission model, which is then optimised via ‘unbinned maximum-likelihood analysis’. From this optimised model, flux measurements are taken, and an LC constructed. This section describes the data cuts applied (§3.1) preceding LC construction (§3.2), and details the choices made to minimise errors and processing time. §3.3 describes virtual sky model problems and solutions.

3.1. Data Cuts

Data cuts that precede *Fermi* analysis (§3.2) are described here. *Fermi*-LAT has an instantaneous field of view of $\sim 20\%$ (2.4 sr at 1 GeV [55]), achieving full sky coverage every ~ 3.2 hrs

¹³ <https://fermi.gsfc.nasa.gov/ssc/data/analysis/documentation/>

¹⁴ <https://fermipy.readthedocs.io/en/latest/>

TABLE II: Blazar properties and associated errors including redshift, SMBH mass, and BL Lac Classification are displayed. Low-luminosity (§1.1) high-synchrotron peaked (HSP) BL Lacs are necessarily low redshift such that they are detectable by *Fermi*-LAT. For clarity, TS , V_{4FGL} and V_2 , defined in §2.3, are rounded to 3 significant figures. Fig. 3 plots SMBH mass against redshift.

Alias	FSRQs	z^a	$\log(M_{BH}/M_\odot)$	Classification ^b	M_{BH}	Ref(s). ^c	TS	V_{4FGL}	V_2
F1	3C 454.3	0.859001(170)	9.0(2)	-	[66, 70] & Refs. therein	444	50900	132000	
F2	3C 279	0.5362(4)	8.8(1)	-	[66, 71, 72]	200	5670	16300	
F3	PKS 1510-089	0.359999(63)	8.4(3)	-	[66]	233	4420	21200	
F4	PKS 1502+106	1.83795(20)	8.9(1)	-	[67, 68, 73]	203	13200	22900	
F5	CTA 102	1.032(3)	8.8(1)	-	[68, 74, 75]	199	14300	25300	
F6	4C+38.41	1.81309(5)	9.43(25)	-	[66]	154	4750	8940	
<hr/>									
BL Lacs									
B1	Mkn 421	0.03002(8)	8.4(2)	HSP	[76]	294	1030	2230	
B2	S5 0716+71	0.300	8.9(6)	ISP	[66, 77]	260	1550	5440	
B3	PKS 0426-380	1.111	8.8(2)	LSP	[71, 78]	221	2680	5890	
B4	PKS 0537-441	0.893(1)	8.75(4)	LSP	[79] & Refs. therein	217	6700	9410	
B5	BL Lacertae	0.0686(4)	8.21(41)	ISP	[66]	167	2470	4780	
B6	Mrk 501	0.03366(7)	9.00(8)	HSP	[76]	154	293	578	

^a Redshifts, z , and errors from NASA/IPAC Extragalactic Database (NED), <https://ned.ipac.caltech.edu/>, and the SIMBAD Astronomical Database, <https://simbad.u-strasbg.fr/simbad/>. Where error is quoted in only one database, this measurement is preferred and appended. Where neither database quotes a measurement error, ± 1 greatest sig. fig. uncertainty is assumed hereafter.

^b Entries from Abdo et al. (2010a) [34], which defines Synchrotron Peak frequency cut-offs, ν_{peak}^{sync} , arranging BL Lacs of Low, Intermediate and High Synchrotron peak into their respective classifications; ν_{peak}^{sync} (LSP) $< 10^{14}$ Hz $< \nu_{peak}^{sync}$ (ISP) $< 10^{15}$ Hz $< \nu_{peak}^{sync}$ (HSP). Revised BL Lacertae classification as ISP from Refs. [65, 66].

^c Ryan et al. (2019) [66] derives average black hole mass and associated uncertainty from Refs. [67–69].

(x2 orbits at an altitude \sim 565 km). During this default ‘all-sky-surveying’ mode, *Fermi* ‘rocks’ North and South, relative to the Earth-spacecraft radial vector (the zenith), and perpendicular to the direction of motion, on alternate orbits. The default ‘rocking angle’ is 35° , and is limited to 60° . When there is a Target of Opportunity (ToO), *Fermi* deviates from this observing mode, and is pointed directly towards a target. Thus, a record of *Fermi* location and pointing direction is essential for analysis, and is stored in the ‘spacecraft file’ (*.SC00.fits), in 30s time intervals.

The spacecraft file also stores times of poor data quality, owing to noisy observing conditions. Increased background flux is observed in a region where the Earth’s magnetic field is weakest: the South Atlantic Anomaly (SAA). Here, the inner Van-Allen belts, that magnetically confine energetic protons (amongst other particles), are at their lowest altitude (~ 200 km) [80]. Roughly $\sim 15\%$ of all data is discarded due to *Fermi* passage through the SAA. Moreover, data quality is irregularly affected by on-board spacecraft events; affected data are removed.

The information stored in the spacecraft file, specific to a target of interest, is converted to a more versatile ‘livetime cube’, that can be applied to any target, provided observations are taken over the same time interval. Here, the ‘livetime’ refers to all GTIs (Good

Time Intervals), when data is retained. In creating the livetime cube, a filter expression of `(DATA_QUAL > 0)&&(LAT_CONFIG == 1)` is applied. The former term ensures only GTIs are retained (where `DATA_QUAL == 0` \equiv ‘bad’), and the latter is the ‘science configuration’; (`LAT_CONFIG == 0` \equiv ‘not recommended’). SOURCE class $E > 30$ GeV data preceding MET = 246823875s is contaminated, due to failed issuing of ACD veto signals, and is cut.

In addition to time cuts, limits on energy and zenith angle are applied, as recommended for P8R3_V2 IRFs. A zenith cut of 90° mitigates the effects of Earth Limb emission (that extend up to ~ 500 MeV), when applied in tandem with the 4FGL minimum recommended energy cut, $E_{min} = 100$ MeV. The maximum energy cutoff is 500 GeV. Finally, the rocking angle is limited by the filter expression (`ABS(ROCK_ANGLE) < 52`), which minimises Earth limb emission.

3.2. Analysis Pipeline

`FermiTools` and `fermipy` are installed in Ubuntu 18.04.3, and photon and space-craft .fits files are downloaded from the online *Fermi*-LAT Data Server¹⁵. Data cuts, analysis parameters, and IRF/background files prescribed in §2.2, 2.3, & 3.1 are applied/set/loaded in via the `config.yaml` file (Appendix C). Standard settings to parameters not yet mentioned are then applied: `binsperdec = 10`, sets the number of energy bins per ‘decade’ of energy (i.e. 1 order of magnitude), `binsz = 0.1` sets angular binning size in degrees, and `roiwidth = 15` sets the target-centred sky-map size in degrees (‘ROI’ is ‘Region-Of-Interest’). Unbinned likelihood analysis is then performed, whereby every discrete photon event is inspected and deconvolved. This analysis is suitable for targets (e.g. blazars) exhibiting a ‘low’ number of events.

Pipeline steps are as follows; the `.yaml` file is loaded in `[gta.GTAnalysis(config.yaml)]`, and the virtual sky emission model is created `[gta.setup()]` and optimised `[gta.optimize()]`, thereby applying the `.yaml` settings, and re-fitting source normalisations and spectral indices, where required. Normalisations and spectral indices of the target blazar, isotropic, and Galactic diffuse models are then freed `[gta.free_source()]`, before optimising the free model parameters `[gta.fit()]`. This maximises the likelihood of obtaining the real data, by varying the virtual sky model, convolving it with the IRF, and measuring the residuals. Following optimisation, a spatial map of residuals is created `[gta.residmap()]`, and visually inspected by the user (§3.3), to ensure the model is reliable. Finally, a light-curve is constructed `[gta.lightcurve()]`.

On inspection, the energy cut-offs must be refined for our 12 sources: despite a maximum *Fermi*-LAT energy range 0.1-500 GeV, the blazar sequence (§1.1) implies flux will peak at a blazar sub-class specific energy. When flux is low ($\sim 10^{-6}$ MeV $cm^{-2} s^{-1}$), upper limits appear in the spectral energy distribution (SED), the errors of which manifest in light curve data points. By limiting energy range, upper limits are cut off, and errors minimised. SEDs are constructed (Fig. 3), and a universal energy range consistent with all 12 blazars, 0.1-10 GeV, is found, and chosen for model creation and LC construction. This also ensures no systematic differences between sub-classes are introduced into the analysis pipeline. In general, SED plots affirm our selection of blazars follow the classical blazar sequence (Figs. 1, 3, more in §6).

¹⁵ https://fermi.gsfc.nasa.gov/cgi-bin/ssc/LAT/LAT_DataQuery.cgi

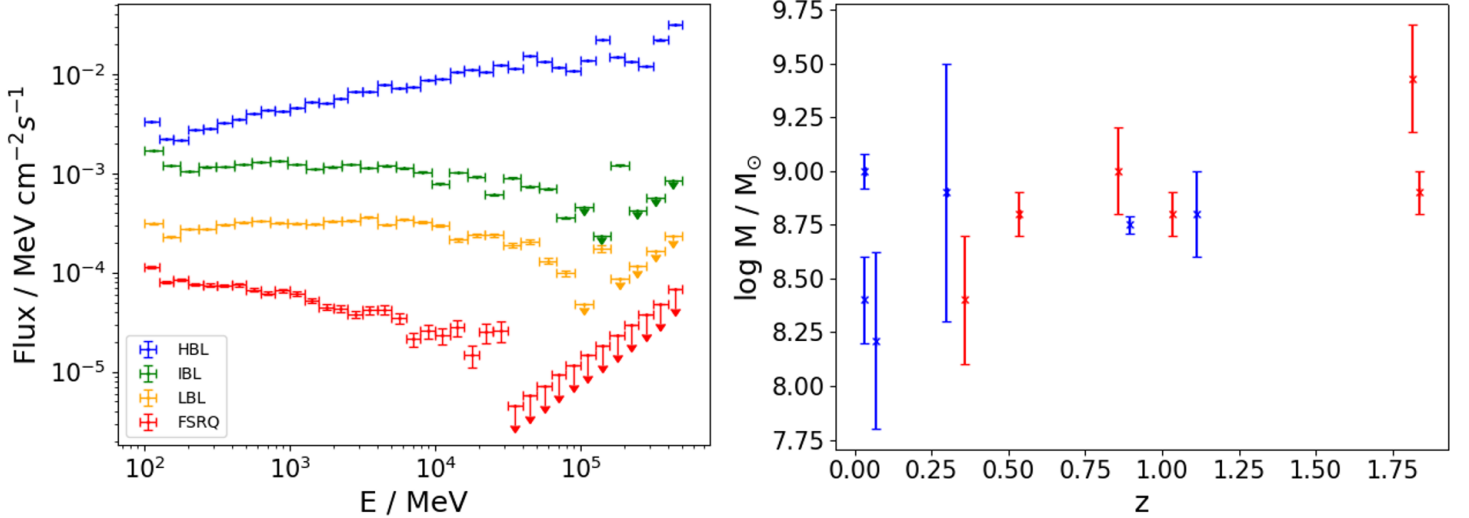


FIG. 3: Plots demonstrate selected blazars likely follow the classical blazar sequence (§1.1). *Left:* 4 of 12 SEDs (offset for clarity): F2 (FSRQ), B3 (LBL), B2 (IBL), B1 (HBL), see Table. II. SED construction from 3 years of data ensures well-characterised targets. FSRQs have the lowest frequency SED peaks (§1.1), and the decaying RHS of the IC peak is observed, with upper limits appearing beyond ~ 10 GeV. BL Lac SEDs are diverse, where the low/intermediate IC peaked BL Lacs exhibit roughly flat spectra, with upper limits introduced from ~ 100 GeV, and the HBLs exhibit a growing SED, with cutoffs > 100 GeV. This motivates a shared energy range for LC construction of 0.1–10 GeV, minimising propagation of upper limits into LC data points. These findings are consistent with the classical blazar sequence. *Right:* Plot shows mass measurements of FSRQs [red] and BL Lacs [blue] against redshift (Table. II). On visual inspection, the selection effects imposed by the *Fermi*-LAT (§1.1) are apparent. At low redshift ($z \lesssim 0.1$), there are a range of observable blazar luminosities. Limited sensitivity ensures only the highest mass blazars are observed at high redshift. Reducing the scatter at low redshift by excluding the high luminosity blazar Mrk 501 (B6, $\log M_{BH}/M_{\odot} \sim 9$), linear fits from chi-squared minimisation universally yield positive gradients (~ 0.1), from selections comprised exclusively of FSRQs, of BL Lacs, and of the remaining 11 blazars collectively. All reduced chi-squared values indicate acceptable fits, with $\chi^2_{\nu} < 1 + 3\sqrt{\frac{2}{\nu}}$ (Eq. 5) [82]. In all, our blazars (perhaps with the exception of B6) likely conform to the classical blazar sequence.

11-year light curves are constructed from 11 discrete 1-year ‘baseline’ models; although time-bin size is arbitrary, empirically¹⁶, this binning is found to strike a good balance between computational efficiency (i.e. minimising the number of virtual sky models created/optimised) while permitting the target to vary sufficiently over the 11-years (the model is time-independent). Similarly, for a given 1-year model, time-binning is a balance of optimising flux errors and ensuring blazar variability is captured (by shortening bin-size), while minimising computation time and ensuring each time bin records an event (by widening bin-size). Weekly-binned LCs are constructed, and upper limits, comprising $\sim 5\%$ of LC points (standard deviation $\pm 4\%$), are

¹⁶ Time bins of (11, 11/3, 1) year and 1 month were experimented with.

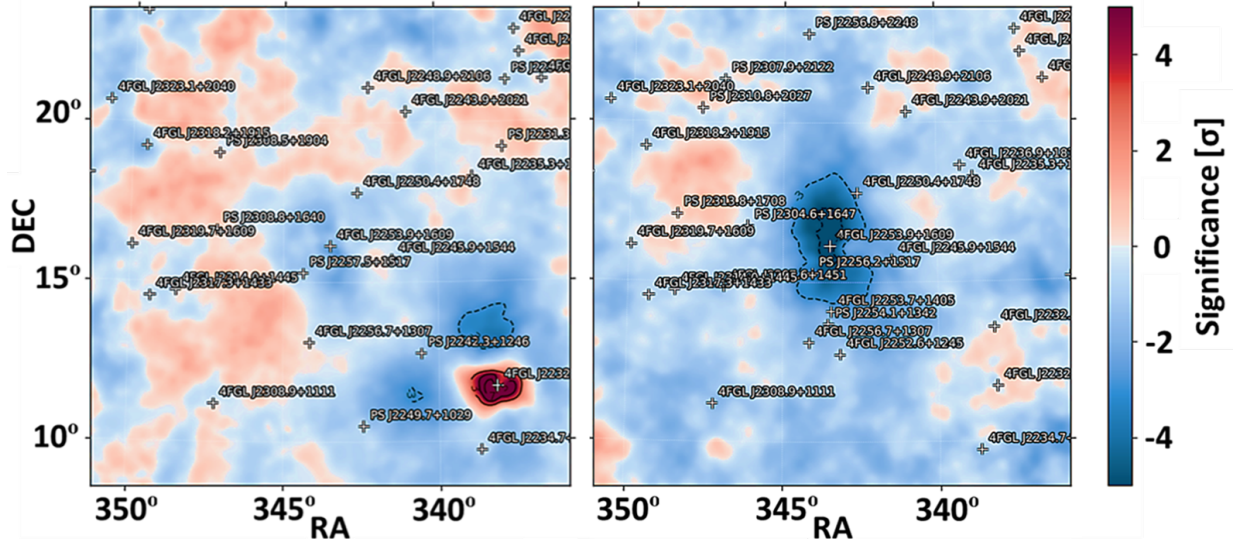


FIG. 4: Residual maps centred on 3C 454.3 showcase poor-fitting virtual sky models. *Left*: Residmap shows off-centre CTA 102 is severely under-fitted ($>5\sigma$), due to low time resolution. *Right*: Residmap shows central target 3C 454.3 is severely over-fitted ($<-5\sigma$), due to large energy-bin size.

removed. Table. III provides LC statistics (example gamma-ray/radio LC pair shown in Fig. 7).

Despite the use of livetime cubes designed to limit the data to GTIs, ‘recent’ data in the time range ~ 58200 - 58400 MJD \equiv March–October 2018 is sporadically corrupted, and gamma-ray LC point time separation universally deviates from ~ 7 days, spiking at ~ 14 - 63 days (example Fig. 7, more in §6). For construction of ‘split-band’ light curves, this motivates a time range limited to ~ 9 years, that does not exceed ~ 58200 MJD. Further, upper limits appear beyond 10 GeV in FSRQs (Fig. 3, §1.1); thus LCs in the range 10-100 GeV are constructed exclusively for the BL Lacs, and for all blazars in the range 0.1-1 and 1-10 GeV.

3.3. Residual Map Solutions

Residual maps (‘residmaps’) describe how well the optimised sky emission model fits the data; intuitively, they can be interpreted as a spatial sky map of some excess, *data – model*, in units of significance, σ (see rigorous definition here¹⁷). Most importantly, fermipy residual map values $> |3\sigma|$ indicate the model is poorly fitted to the data, where red regions indicate the model is ‘under-fitting’ the data, and blue regions indicate ‘over-fitting’. Two major issues, and one minor issue, arose upon inspection of residmaps following the model optimisation process described in §3.2. Firstly, the brightest blazar in the sky, 3C 454.3 (4FGL $TS = 443.8451$), is over-fitted ($<-5\sigma$) under the standard analysis procedure. Secondly, 3C 454.3 and CTA 102 are under-fitted ($>5\sigma$) at ~ 9 -years. Finally, all sources, on occasion, exhibit small levels of under and over-fitting ($\sim |3-5|\sigma$). This motivates a study of the model-fitting procedures. Residmap problems and solutions are displayed in Fig. 4, 5, 6.

¹⁷ <https://fermipy.readthedocs.io/en/latest/advanced/residmap.html>

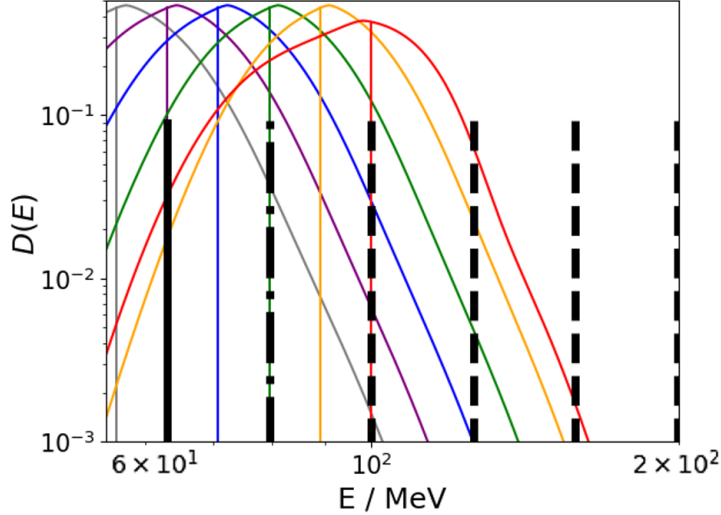


FIG. 5: Colour plots show energy dispersion function, $D(E)$ (prescription in Appendix C), where vertical colour lines indicate true incident photon energy $E = E_\gamma$, and function indicates the probability of measuring $E = E'_\gamma$. Vertical dashed lines indicate bin sizes under `binsperdec` = 10, dot-dash line marks the ‘next-lowest-bin’ (under the low E limit 100 MeV), and black solid line shows the alternative ‘next-lowest-bin’ under `binsperdec` = 5. On inspection, the lowest true energy photons inferred are $E=100^{0.95}$ MeV \approx 79.4 MeV [green]. Thus any blue/purple E_γ photons with E'_γ that leaks into the range $E > 100$ MeV are modelled as some $E_\gamma \gtrsim 79.4$ MeV photon, leading to an over-abundance in this range. By lowering `binsperdec` (to e.g. 5), blue/purple photon true energy is appropriately inferred, and source model does not over-fit the data.

In order to address 3C 454.3 over-fitting, the function, $D(E)$, describing energy dispersion (Appendix. C) is inspected, in addition to the Fermitoools analysis procedure. When deconvolving measured energy, E'_γ , with the IRF, the Fermitoools scripts automatically employ the ‘next-lowest-bin’ in energy. As shown in Fig. 5, a `binsperdec` parameter too small, by comparison with typical energy dispersion width, leads to over-fitting. For 3C 454.3, this effect is significant due to the over-abundance of incident photons (particularly at low energies, that suffer high energy dispersion; see Fig. 3 for FSRQ example, and §3.2 on Data Resolution). A `binsperdec` setting of 4 is employed over the majority of the 11-year data series, to mitigate the effects of over-fitting. In general, all instances of over-fitting are solved by employing $\text{binsperdec} < 10$. Fig. 6 showcases this solution in action.

By contrast, instances of under-fitting are *not* solved by increasing `binsperdec`. Instead, the time-independence of the sky model is responsible: if a blazar flares rapidly over the analysis time (1-year), the time-independent flux model under-predicts blazar activity (Fig. 4). This is solved by implementing 1-month time intervals under normal analysis procedures.

4. SUB-MILLIMETER ARRAY DATA & RADIO LIGHT CURVES

Radio observations of blazars from \sim 2002-2019 are made with the Sub-Millimeter Array (SMA), a radio interferometer observing in the range 180-900 GHz (1.7-0.3 mm), that consists

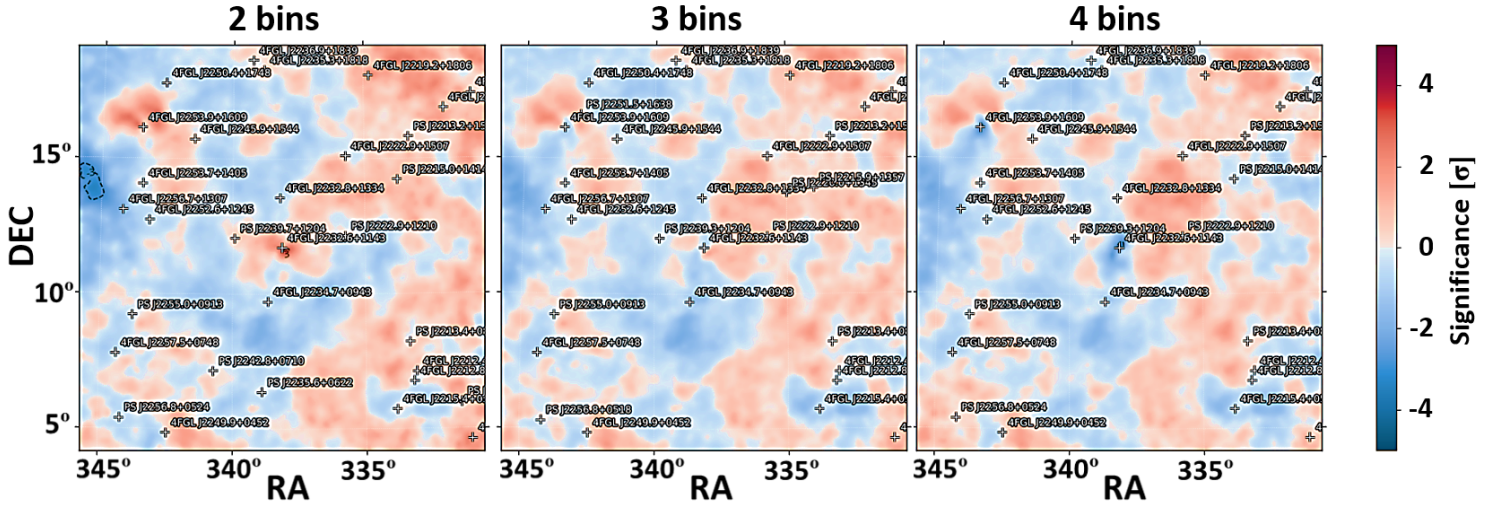


FIG. 6: Residual maps centred on CTA 102 during MJD~58052-58417 showcases influence of binsperdec on model fitting. Target exhibits high activity, which leads to over-fitting under binsperdec = 10. Plots from left to right show residual maps under binsperdec settings of (2,3,4), respectively; this leads to model under-fitting, optimisation and over-fitting.

of eight 6m-diameter antennae located near the summit of the dormant volcano Mauna Kea in Hawaii ($19^{\circ} 49' 27.48''$ N, $155^{\circ} 28' 40.8''$ W) [83]. This section briefly describes how SMA data is acquired to construct light curves. Data taken from the Submillimeter Calibrator List¹⁸ (Table. III), comprises observations of >400 blazars in the ‘1mm’ and ‘850 μ m’ bands (§4.2).

4.1. Data Acquisition

Formally commissioned on November 22nd 2003, the SMA was the world’s first dedicated interferometer observing at sub-millimeter wavelengths, improving upon the angular resolution of its single-aperture predecessors by a factor of 30 [83]. Optimised with neural network algorithms, the SMA array design leads to effective baselines of 9-500m, corresponding to 0.5-0.1” resolution from 200-850 GHz [84]. Blazars, with sizes $< 0.01''$, thus appear as point sources (such that geometric time delay is known) [85]. Radio waves are collected by discrete movable antennae, each of which has a primary and secondary machined-cast aluminium reflector, directing waves towards a central receiver. Appendix. D provides more detail on radio wave collection/processing, and details the motivation behind the array design [83, 84, 86].

Blazars are employed as phase and amplitude gain ‘calibrators’ by the Smithsonian Astrophysical Observatory (SAO), to characterise and mitigate the effects of atmospheric water vapour and absorption [85, 87–89]. Water vapour has a refractive index $n > 1$ (that increases with density), causing a time delay, thereby imprinting an additional phase on transiting radio waves. Vapour density is rapidly variable (from ~ 1 hr to < 1 s timescales), requiring that phase and amplitude corrections are continuously applied [85, 88, 89]. Calibrator blazars act as guide

¹⁸ <http://sma1.sma.hawaii.edu/callist/callist.html>

stars (analogous to laser guide stars for adaptive optics), allowing atmospheric effects to be sufficiently characterised within a 3-5 minute blazar exposure [90, 91]. Selected blazars are bright (minimum 230 GHz flux $> 750 \text{ mJy}$ and 345 GHz $> 1 \text{ Jy}$ [92], $1\text{Jy} = 10^{-26}\text{Wm}^{-2}\text{Hz}^{-1}$), ensuring a sufficient SNR is achieved in an exposure time less than the timescale for atmospheric variability [89]. Moreover, blazars are readily identifiable, with well defined locations ($<20\text{mas}$), and are thus ideal calibrators [87, 89].

4.2. Data Resolution & Light Curve Construction

Of importance for light curve construction are blazar flux densities and their associated uncertainties. The popular SMA observing site (home to a total of 13 telescopes) is extremely dry, meaning sub-millimetre attenuation/phase error due to water vapour is minimised [90]. Nonetheless, despite accounting for the geometric time delay and global phase offset due to water vapour, a non-negligible r.m.s phase error arising from rapid atmospheric fluctuations manifests as a flux density uncertainty [83, 88, 93]. Time delays associated with electrical and opto-mechanical effects, introduced by signal processing/instruments, also contribute towards data point uncertainty [88]. Finally, there is uncertainty in the absolute flux scale, derived from observations of Solar system objects (most often Callisto, Ganymede, Neptune, Titan, and Uranus). These are selected for flux calibrations because they are well studied, with accurate ($<5\%$ error) flux models [83, 85, 87, 89, 93].

Blazars are observed in the ‘1mm’ and ‘ $850\mu\text{m}$ ’ bands, which range $\sim(1.1\text{-}1.4)\text{mm}$, and $\sim(850\text{-}900)\mu\text{m}$, respectively. The amount of data in the latter band is far exceeded by that in the former, by a typical factor ~ 20 for our sources (Table. III), and thus, is ignored. ‘1mm’ band data, comprising radio flux, error, frequency, and date of observation, are downloaded as a .txt files from the SMA Calibrator list. Utilising the calendar module in Python, date is converted from the Gregorian calendar to Modified Julian Day (MJD), zeroed at 12am on 17th November 1858. A convenient local time-stamp is 00:00:00 01/01/08 $\equiv 54466$ MJD. Fig. 7 displays an example SMA light curve, and LC statistics are displayed in Table. III.

5. CORRELATION ANALYSIS

Following construction of 12 11-year pairs of gamma-ray (§3) and radio (§4) blazar light curves (Table. III), correlation analysis is performed, to search for significant correlations, and quantify time-lags, between these extreme-energy wavebands (e.g. Fig. 7). The Discrete Cross Correlation Function (DCCF) is a tool widely employed to search for significant correlations (and/or anti-correlations) between two irregularly sampled light curves: $(\{x_i(t_i)\}, \{y_j(t_j)\})$ [28, 37–40, 94]. Where significant correlations are found, the time-lag, $\tau = t_j - t_i$, can be estimated. §5.1 provides a prescription of these analysis methods. §5.2 details confidence tests for accepting/discardng significant correlations, and displays results of correlating 0.1-10 GeV gamma-ray and ‘1mm’ band radio LCs. §5.3 performs analysis on split-band gamma-ray LCs.

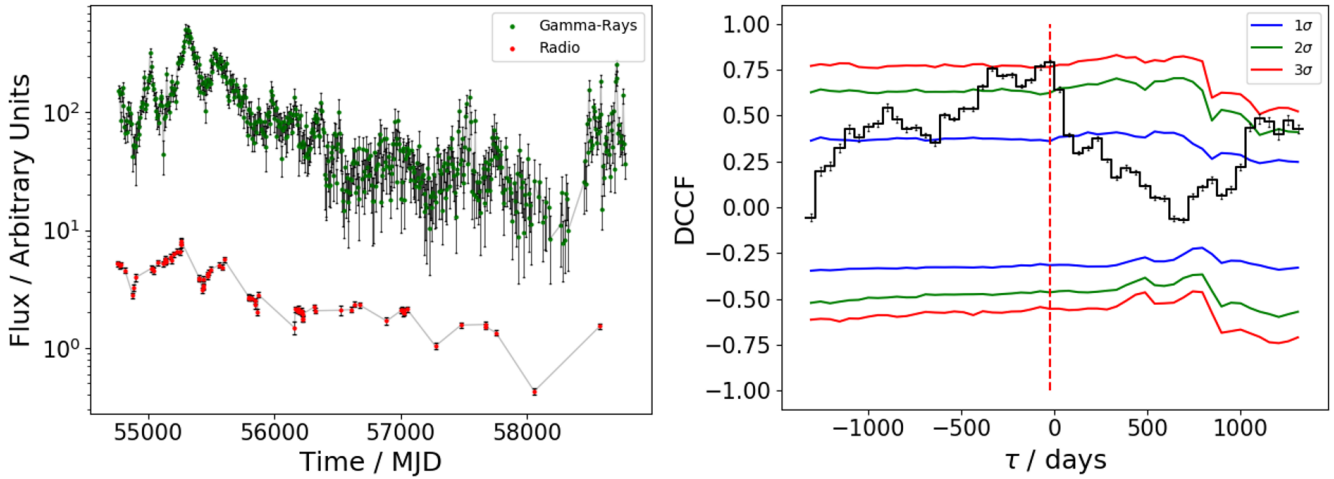


FIG. 7: PKS 0537 - 441 light curves and raw DCCF displayed. *Left:* Upper weekly-binned gamma-ray LC [green] is well sampled, except for regions of corrupt data points (§3.2), with points noticeably absent at ~ 58300 MJD (§6). Lower radio LC [red] appears correlated, and has a moderate level of clustering, 89 d (Table. III). In particular, although flare rises appear well-sampled, flare decay LC points are absent. This could bias the DCCF towards a radio-leading time lag. *Right:* The corresponding DCCF (confidence levels of (1, 2, 3) σ [blue, green, red] displayed), yields a maximum significant peak, $3.25^{+0.45}_{-0.20} \sigma$, in the τ -bin centred on $\sim - 26$ d, implying a radio-lead. Qualitatively though, we see the DCCF is high-valued for $\tau < 0$, and low valued for $\tau > 0$, which is likely a consequence of the chance radio sampling. This example serves to illustrate the DCCF is not wholly reliable, and that in general, radio sampling/clustering must be evaluated when accepting/discardng DCCF results.

5.1. DCCF & Lag Measurement Prescription

To construct the DCCF, firstly, the Unbinned Cross Correlation Function (UCCF) is found;

$$UCCF_{ij}(\tau) = \frac{(x_i - \bar{x})(y_j - \bar{y})}{\sigma_x \sigma_y}. \quad (4)$$

Here, \bar{x} and σ_x are the mean and standard deviation of some selection of fluxes, $\{x_i\}$. The DCCF is created by averaging the UCCF points in bins of τ . For a given τ bin, the mean and standard deviation in Eq. 4 is calculated exclusively with the contributing LC points¹⁹, such that $|DCCF| \leq 1$. A DCCF peak close to (-)1 indicates a significant (anti-)correlation. Following Ref. [28], range in τ is chosen so 2/3 of the light curves are overlapping; for ~ 11 -year LCs, this gives $|\tau| \lesssim 1350$ d, a range in excess of literature lag measurements (Table. I), that should encompass all significant lags. The τ bin-size is set to the average cadence of the lower sampled LC [28]. For LC analysis over a limited time range, perhaps sampled at a higher-than-average cadence, a higher resolution/smaller bin-size in τ could be employed; in general though, our analysis is limited to the full time-series, and average cadence is most suitable.

On identification of a DCCF peak (significance measures in §5.2), the lag and associated error must be determined. Following Refs. [28, 37, 40], we model the DCCF peak as a Gaussian,

¹⁹ Formally then, the DCCF takes the form of the ‘Local Cross Correlation Function’ (hereafter, ‘DCCF’) [95, 96].

TABLE III: Table of LC statistics show; 11-year LC mean flux and standard error, $\bar{F}(\pm\alpha_{\bar{F}})$ [*Fermi*] LCs in 10^{-5} MeV cm $^{-2}$ s $^{-1}$, SMA LCs in Janskys: 1Jy = 10^{-26} Wm $^{-2}$ Hz $^{-1}$], Variability index (Eq. 3), V , and number of data points, N . LC consistency with the null hypothesis (of a constant flux) is tested, and quantified in the X column (3 sig. fig.); defining $\sigma = \sqrt{2\nu}$, $\chi^2_{min} = \nu + X\sigma$ [38, 82]. SMA ‘Clustering’ column shows the standard deviation of LC neighbouring-point time-separations, to the nearest day. Number of data points in *Fermi* LCs vary due to failed weekly bins and removal of upper limits. In particular, 3C 454.3 LC has \sim half as many LC points as other *Fermi* LCs, which is discussed in §6. Number of data points in the 1mm and 850 μ m bands shows over-abundance of the former (§5.3). *Fermi* average LC data point uncertainty is high, $\sim 22 \pm 7\%$, as compared with $\lesssim 10\%$ energy dispersion, and SMA LCs: $6 \pm 1\%$. Radio LCs suffer from a high degree of clustering, whereby closely grouped collections of data points are widely separated (Appendix. G), More in §5.2 and §6.

		<i>Fermi</i> -LAT				Sub-Millimeter Array						
Alias	FSRQs	$\bar{F}(\pm\alpha_{\bar{F}})$	V	N	X	$\bar{F}(\pm\alpha_{\bar{F}})$	V	Clustering / d	N_{1mm}	$N_{850\mu m}$	X	
F1	3C 454.3	46(3)	0.999	257	1424	15.6(3)	0.958	19	902	212	3240	
F2	3C 279	23(2)	0.991	557	1036	10.8(2)	0.612	20	672	94	506	
F3	PKS 1510-089	24(1)	0.974	552	823	1.80(5)	0.693	39	198	12	331	
F4	PKS 1502+106	10.5(5)	0.98	472	426	1.32(7)	0.837	100	104	8	746	
F5	CTA 102	20(2)	0.994	496	1014	3.0(2)	0.827	58	202	29	723	
F6	4C+38.41	8.8(4)	0.969	506	377	2.18(8)	0.722	37	203	22	463	
		BL Lacs										
B1	Mkn 421	12.8(3)	0.881	544	87.0	0.27(1)	0.259	133	71	4	22.7	
B2	S5 0716+71	10.4(3)	0.964	539	265	2.77(9)	0.866	17	378	27	869	
B3	PKS 0426-380	11.5(8)	0.997	533	232	1.56(8)	0.734	111	81	3	288	
B4	PKS 0537-441	8.5(4)	0.96	514	212	3.6(2)	0.886	89	91	1	646	
B5	BL Lacertae	12.7(4)	0.96	531	244	5.0(2)	0.844	21	477	88	1046	
B6	Mrk 501	3.8(1)	0.856	516	21.5	0.45(1)	0.160	123	60	7	11.2	

optimise the fit via chi-squared minimisation, and extract best fitting values, and associated errors from the curvature matrix [82, 97]. However, choice of τ error is not obvious. Empirically, the Gaussian mean uncertainty, α_τ , and the Gaussian standard deviation σ_τ , are found to be excessively small/large, respectively, of the order ~ 1 and 1000% of τ . Thus, tests are performed to determine the optimum choice of error, amongst: α_τ , σ_τ , and the DCCF bin-size, b_τ .

For each blazar, 1000 fake radio LCs are constructed. A fake radio LC is a randomly time-offset gamma-ray LC with points deleted, such that the resulting LC shares the same clustering profile as the real radio LC. If no real gamma-ray point is available (due to high radio clustering), new LC points are created via linear interpolation, from one real point to the next, and the mean error of the two is applied. By feeding the fake radio and real gamma-ray LC into the DCCF recipe, the real lag, the inferred lag, and the error are known²⁰. Thus the number of errors, X , from the inferred lag to the real lag, can be determined. In a perfect setup, 68% of cases would be contained by $X \leq 1$. However, LC structures in a given real-gamma/fake-radio pair differ,

²⁰ This exercise also serves to affirm the DCCF code functions as intended.

and they do not yield Gaussian shaped DCCF peaks, as is true for e.g. sinusoids. Moreover, the *real* radio structure necessarily deviates from that of the fake radio. Thus, as a fail-safe, 100% containment is applied for optimising error choice.

For all 12 blazars, b_τ is optimum; it is always an over-estimate, unlike α_τ , but is preferred over σ_τ , which is excessively large²¹. Employing b_τ , 100% containment level universally resides in the range 0.1-1. These results are independent of the goodness-of-fit, regardless of whether $\chi_\nu^2/\chi_{\nu-\max}^2$ is greater or less than 1. We define the largest acceptable χ_ν^2 value [82]:

$$\chi_{\nu-\max}^2 = 1 + 3\sqrt{\frac{2}{\nu}}. \quad (5)$$

5.2. Confidence Tests & Results

By quantifying the significance of a DCCF peak, the detection of chance correlations, whereby multiple pairs of causally unrelated flares can produce a DCCF spike, can be minimised. Confidence intervals are employed to accept or discard a DCCF peak, and a threshold confidence level for a significant correlation is chosen to be $>3\sigma$, following Refs. [28, 37, 38]. By synthesising gamma-ray LCs (see below), and correlating each synthetic LC with the real radio LC, a list of DCCF points for each τ bin, $DCCF_\tau$, is created, and ordered by numerical value. Splitting into positive (correlation) and negative (anti-correlation) lists, $DCCF_{\tau,\pm}$, levels of $X\sigma$ can be estimated, with DCCF height:

$$Confidence_\pm(\tau, X) = \begin{cases} DCCF_{\tau,+} \left[len(DCCF_{\tau,+}) \cdot erf\left(\frac{X}{\sqrt{2}}\right) - 1 \right] \\ DCCF_{\tau,-} \left[len(DCCF_{\tau,-}) \cdot (1 - erf(\frac{X}{\sqrt{2}})) \right] \end{cases}. \quad (6)$$

List length is $len(DCCF_{\tau,\pm})$, square brackets enclose list index, ranging 0 to $len(DCCF_{\tau,\pm}) - 1$, and error function, erf , assumes Gaussian distributed probabilities (§6). The resolution in significance thus depends on the number of synthetic LCs.

To synthesise light curves, firstly, the method of Timmer & Koenig (1995) was tested²² (hereafter, ‘TK95’) [98]. On inspection, the synthetic LCs match the real LC power spectral density (PSD), however they show no ‘structure’ (e.g. flaring/outburst activity), and are restricted to ‘flicker’ over the 11-year time series. Resulting confidence intervals exhibit erratic fluctuations, with relative standard deviation (RSD), $67 \pm 21\%$, and structure governed by the radio light curve. In all, contours generated under TK95 are unreliable.

Emmanoulopoulos (2013) (hereafter, ‘E13’) [99], identify that TK95 is suitable only for synthesising LCs with a Gaussian probability distribution function (PDF), and note real AGN LCs typically exhibit non-negligible probabilities for large flux values (that exceed those permitted by a Gaussian PDF). Thus, E13 modifies the TK95 method by fitting the PDF, in addition to the PSD. Unlike TK95 though, the E13 prescription requires an evenly sampled input light curve.

²¹ A fourth option would be to select an error range equal to the DCCF span above the 3σ confidence level.

Necessarily though, this will always be greater than or equal to the bin-size, so need not be tested.

²² This method models the power spectral density (PSD) with a power-law, multiplies model values by Gaussian drawn random numbers, and uses these values to construct a complex Fourier-transformed synthetic LC.

For our weekly-binned gamma-ray LCs, this condition is mostly satisfied, except for small regions of corrupt data points (see §3.2, e.g. Fig. 7). These regions are linearly interpolated in Python, and the resulting LCs are fed into the publicly available E13 package²³ [100]. E13 synthetic LCs match the real PDF and PSD, and exhibit flares and periods of outburst. Moreover, the contours show reduced structure, with RSD $10 \pm 5\%$. Confidence intervals generated under E13 are reliable, and 10,000 LCs per blazar are synthesised. Empirically, this allows for 0.01σ resolution in significance up to $\sim 8\sigma$, beyond which peak significance cannot be resolved.

Confidence intervals are the most effective means of identifying significant (anti-)correlations, however, DCCF outputs cannot be accepted without further evaluation. Additional tools to evaluate DCCF results include: *i*) colour maps of LC points contributing to $|UCCF| > |DCCF|$, *ii*) success rates for correctly identifying the true underlying correlation, *iii*) consideration of radio sampling, clustering and consistency with the null hypothesis, and *iv*) DCCF predictions based off LC visual inspection. While none of these tools individually yield conclusive results, collectively they are employed to draw informed conclusions.

Firstly, colour maps are constructed. On identifying the most significant DCCF peak, the DCCF recipe is reverse-engineered, locating and plotting all LC point pairs that contribute to $|UCCF| > |DCCF|$. The case of 3C 454.3, explored in Fig. 8, highlights the importance of these colour maps, showcasing that, in general, the most significant DCCF peak may be false.

Secondly, given maximum DCCF peaks can misrepresent the true underlying correlation (or lack thereof), success rates for correct identification of the maximum DCCF peak (i.e. correct τ bin, correct correlation type) can be calculated with simulated LCs, and used as an indicator of DCCF reliability. Appendix. E prescribes methods for synthesising LCs and calculating success rates with Bayes' Theorem; success rate results are plotted and discussed in Fig. 9. When projecting success rates onto the real LC-pair DCCF, the underlying assumption is that, like the fake (anti-)correlated pairs, they are coupled by a single unique time lag. However, real LCs could exhibit a mix of lags. Thus, success rates should be employed only as an indicator.

Thirdly, success rate findings are supported/dismissed by cross-referencing with radio sampling, clustering, variability index, and consistency with the null hypothesis (explored fully in Appendix. F, findings are tabulated in Table. III). Radio sampling (N) and clustering (Cl) are rough proxies for one another (e.g. anti-correlation between clustering and N_{1mm} in Table. III). Similarly, the measure of consistency with the null hypothesis (X) is roughly correlated with the variability index (V). Grouping (V, X) and (Cl, N), both weakly correlate with total success rate. In practice, such relations are utilised only on consideration of extreme examples. Most notably, B6 has the second highest level of clustering, the lowest N, V, X , and, (likely as a result), the lowest total success rate (Table. III, Fig. 9); this provides confidence in B6 success rates. Similarly, low success rates in B1 and B3 are affirmed. F5, however, is an outlier; although sampling/clustering is favourable over that of e.g. F4's, it's total success rate is surprisingly low ($65 \pm 2\%$). Coupled with a good un-correlated success rate of $94 \pm 2\%$, this implies only correlations/anti-correlations are unsuccessful. On further inspection, a 3-pronged

²³ <https://github.com/samconnolly/DELightcurveSimulation>

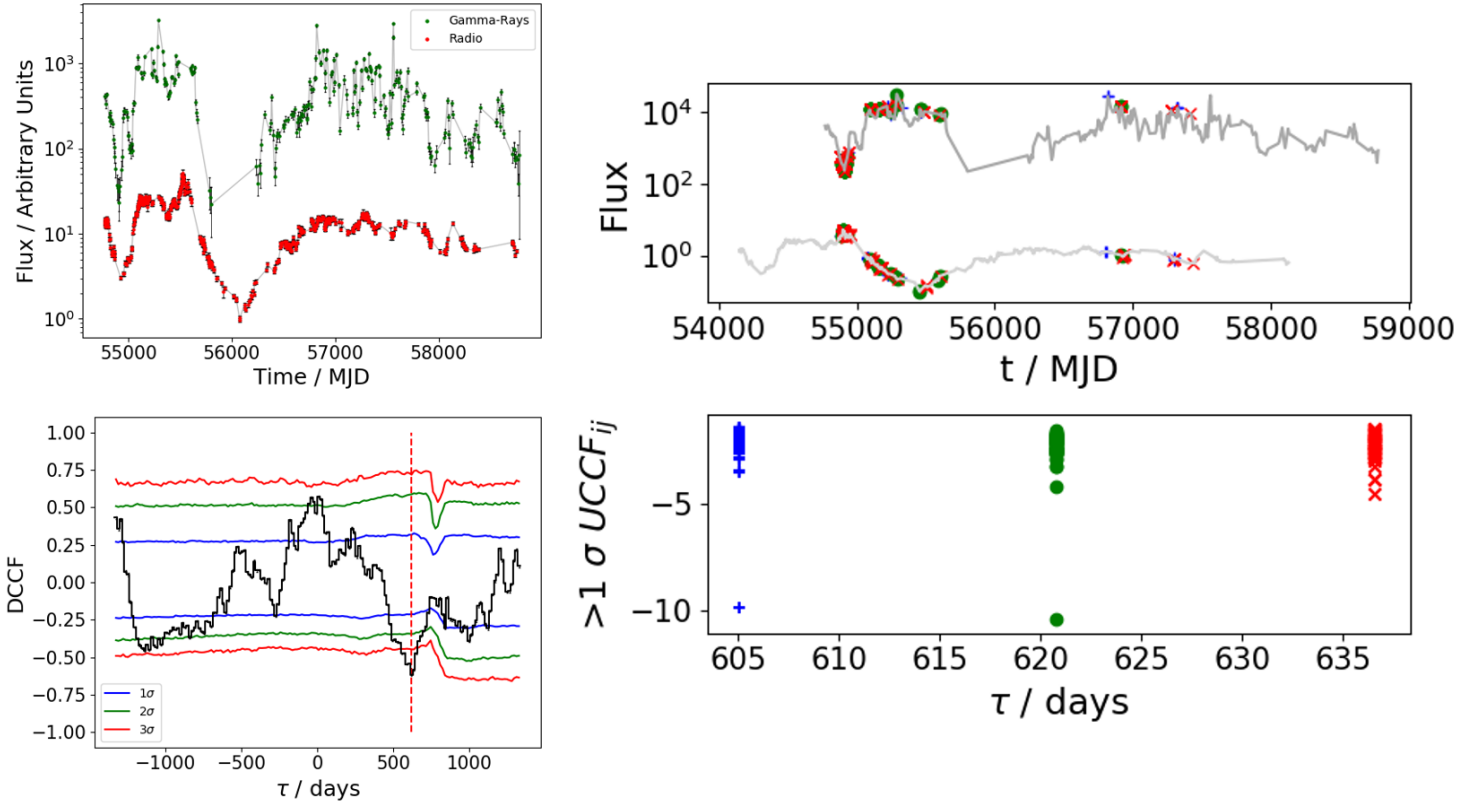


FIG. 8: Plots demonstrate LC pair analysis with colour maps ($|UCCF| > 1\sigma + |DCCF|$ chosen for clarity). *Upper Left:* LC pair is, on visual inspection, correlated by some lag of the order 10's of days. *Lower Left:* DCCF shows a significant broad anti-correlated peak at $\tau \sim 620$ d, contrary to expectations following LC inspection. *Right Panels:* Unique markers/colours highlight both the $> 1\sigma$ UCCF points in significant DCCF τ -bins, and the LC points that contribute towards each UCCF point. Radio LC is offset by the inferred lag, revealing the anti-correlation is fake. Just as a pair of sinusoids are significantly correlated at a lag, $\tau = \phi$, so too are they significantly anti-correlated at $\tau = \phi + \pi$. Outburst period of 3C 454.3 is apparently anti-correlated with subsequent period of quiescence. In general, DCCF peaks must be inspected with colour maps, and cross-referenced with our expectations.

structure in the DCCF is typical, where the central prong is *always* the true lag, and in \sim half of cases, the inferred lag is one of the other two. This 3-prong structure manifests in the real DCCF (central prong is maximum). This indicates a mix of lags/periodicity in F5, accounts for low success rates, and re-affirms the maximum peak does not always represent the true correlation.

Finally, visual inspection of LCs/DCCFs is an invaluable tool. As evidenced by Figs. 7, 8 and the discussion above, results are readily accepted/discredited depending on whether DCCFs align with expectations following LC inspection. Blazars are inspected individually, with notes detailed in Appendix F. Results are collated and evaluated in Table IV, including a calculation of $\Delta r_{r,\gamma}$ (Eq. 1). Of the few lags measured, no dependence on mass is found. In general, blazars requiring further investigation are those exhibiting maximal, $< 3\sigma$, DCCF peaks, aligned with expectations. Failure of peak significance to exceed 3σ is accounted for in §6.

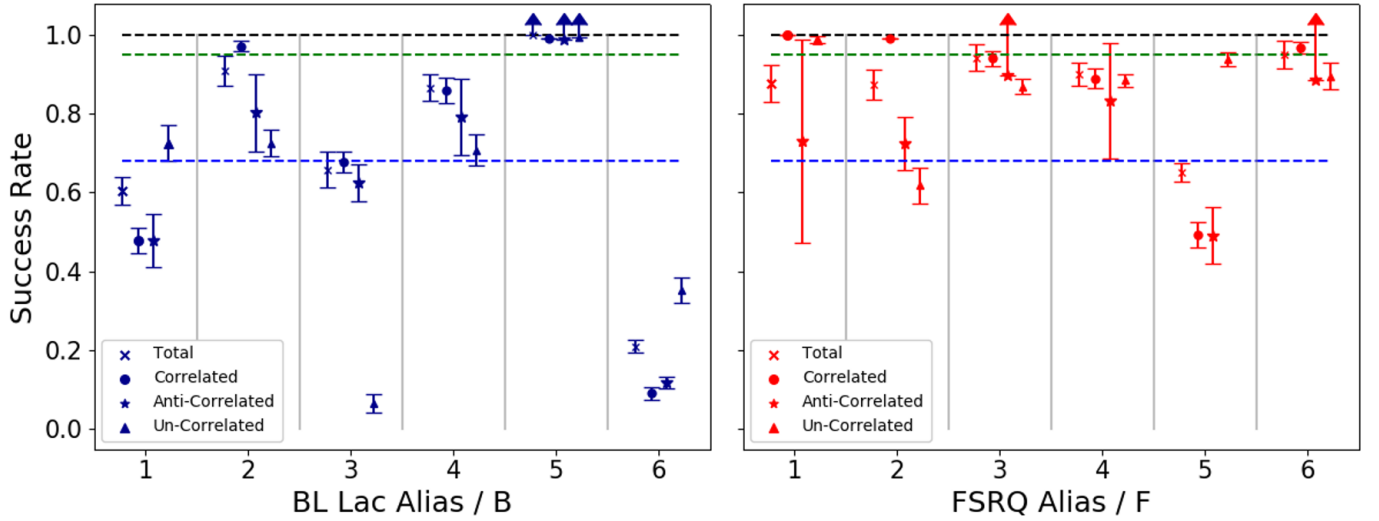


FIG. 9: Blazar success rates of light curve pairs (γ -ray + synthetic) found to be correlated [circle], anti-correlated [star] and un-correlated [triangle] are plotted (aliases in Table. II, (68,95,100)% [blue, green, black] dashed lines plotted). A success is defined as identifying a maximum $>3\sigma$ DCCF peak (or lack thereof) in the correct τ bin, with a correlation type that matches the true underlying correlation. For each blazar, 10 iterations of 300 simulations are performed, applying an underlying true correlation (x100), anti-correlation (x100) and no correlation (x100) between light curve pairs. Findings are blazar specific, and are generally governed by radio sampling. For example, owing to the excellent radio sampling (Table. III, Appendix. F), B5 DCCFs are reliable with a total success rate $>99.7\%$. By contrast, success rates of B1 and B6 are poor ($<68\%$), and B3 (anti-)correlations are frequently lost (un-correlated success rate $7\pm2\%$). FSRQ success rates are moderate $\cong 1-2\sigma$, bar F5, that exceeds 68% only when the DCCF exhibits no correlation (see text). These findings aid in evaluating real DCCFs.

5.3. Split-Band Analysis

In addition to 11-year 0.1-10 GeV gamma-ray LCs, correlation analysis is performed on weekly-binned ~ 9 year ‘split-band’ LCs, in the ranges (0.1-1, 1-10) GeV (and 10-100 GeV in BL Lacs, §3.2). On visual inspection, all LC pairs of 0.1-1 and 1-10 GeV are correlated, at some small lag of the order $|\tau| \sim 1$ d. Applying the same DCCF τ -bin settings as in §5.1, the peak lag is universally consistent with $\tau = 0$. Motivated by LC visual inspection and physical intuition, significance tests are unnecessary to affirm these peak lags are not false positives. DCCF bin-size is ~ 7 d in all cases, and thus we can place an upper limit $|\tau| \lesssim 7$ d on LC pairs of 0.1-1 and 1-10 GeV. Excluding B1, BL Lac 10-100 GeV LCs universally show consistency with the null hypothesis ($\chi^2_\nu < 1$), and are ignored. B1 DCCF of 0.1-1 and 10-100 GeV is again consistent with a zero lag, and the 7 day upper limit is applied. Although visual inspection generally implies high-energy leads, as expected from the shock-in-jet scenario, DCCF utility has been exhausted, given an input of weekly-binned LCs. With daily binned LCs, perhaps DCCFs would reveal whether high-energy truly leads.

A new and potentially viable method is devised and experimented with to yield finer lag

TABLE IV: Results of correlation analysis are tabulated. ‘Conclusion’ column indicates whether analysis is complete and conclusions are robust (✓), if analysis is incomplete and/or conclusions are preliminary (~), or else if data has been exhausted, and more information is required (X). Inferred ‘Correlation’ is correlated (C), anti-correlated (AC) or un-correlated (UC). Where lag is neither radio (R) nor gamma-ray (γ) leading, ‘Lead’ is denoted ‘?’ . FSRQ results generally indicate a gamma-ray leading correlated lag, of order 10’s of days, in 4/5 of 6 sources. F1 exhibits a double peak (Appendix. F). LBLs are likely correlated, but with radio leading lags, IBLs are diverse, and HBLs are low variability, and poorly sampled, allowing no firm conclusions to be drawn (§6). Most interestingly, a highly significant anti-correlation is found in B2, under a limited time range $t < 56800$ MJD. Eq. 1 physical parameter data is taken from Ref. [65]; data on B3/B4 is absent.

Alias	FSRQs	Conclusion	Correlation	Lead	Peak	Significance / σ	$\tau \pm \alpha_\tau$ / d	$\Delta r_{r,\gamma}$ / pc
F1	3C 454.3	~	C	?	>2	-16±47	-2±7	
F2	3C 279	✓	UC	-	-	-	-	
F3	PKS 1510-089	~	C	γ	$2.52^{+0.15}_{-0.07}$	28±11	22±8	
F4	PKS 1502+106	~	C	γ	$1.85^{+0.08}_{-0.04}$	84±52	14±9	
F5	CTA 102	~	C	γ	$2.27^{+0.13}_{-0.05}$	55±15	3.1±0.9	
F6	4C+38.41	✓	C	γ	>8.38	23±13	9±5	
<hr/>								
	BL Lacs							
B1	Mkn 421	X	UC	-	-	-	-	
B2	S5 0716+71	~	AC	R	>8.38	-20±6	-8±2	
B3	PKS 0426-380	~	C	R	$2.62^{+0.32}_{-0.13}$	-57±35	-	
B4	PKS 0537-441	✓	C	?	$3.25^{+0.45}_{-0.2}$	-60±117	-	
B5	BL Lacertae	✓	UC	-	-	-	-	
B6	Mrk 501	X	UC	-	-	-	-	

resolution with weekly binned LCs. Cubic interpolation²⁴ on a well-sampled LC yields a continuous function, that can be resolved to an arbitrarily high resolution. By minimising,

$$\text{Integral}(\tau) = \int_{t_1}^{t_2} \left| \frac{LC_1(t + \tau)}{LC_2(t)} \right| dt, \quad (7)$$

over some limited range in t (here $t_2 - t_1 \simeq (2/3)9$ yr), the lag is determined. The underlying philosophy is that if two LCs share the same profile, the integrand is minimised (~1) at the correct lag. This method is compelling, however the choice of resolution must be optimised, and associated errors must be evaluated (as yet LC flux uncertainties are ignored, and only best fit values are employed). Fig. 10 demonstrates preliminary results. Due to time constraints this method is not explored further, and split-band LCs, given their semblance to 0.1-10 GeV LCs, are not correlated with radio LCs. Analysis of 850 μ m radio LCs is reserved for future work.

6. DISCUSSION

This section evaluates flaws in the LC construction/DCCF analysis methods, attempts to physically interpret §5 results (Table. IV), and highlights the vast scope for future work (LC

²⁴ <https://docs.scipy.org/doc/scipy/reference/generated/scipy.interpolate.interp1d.html>

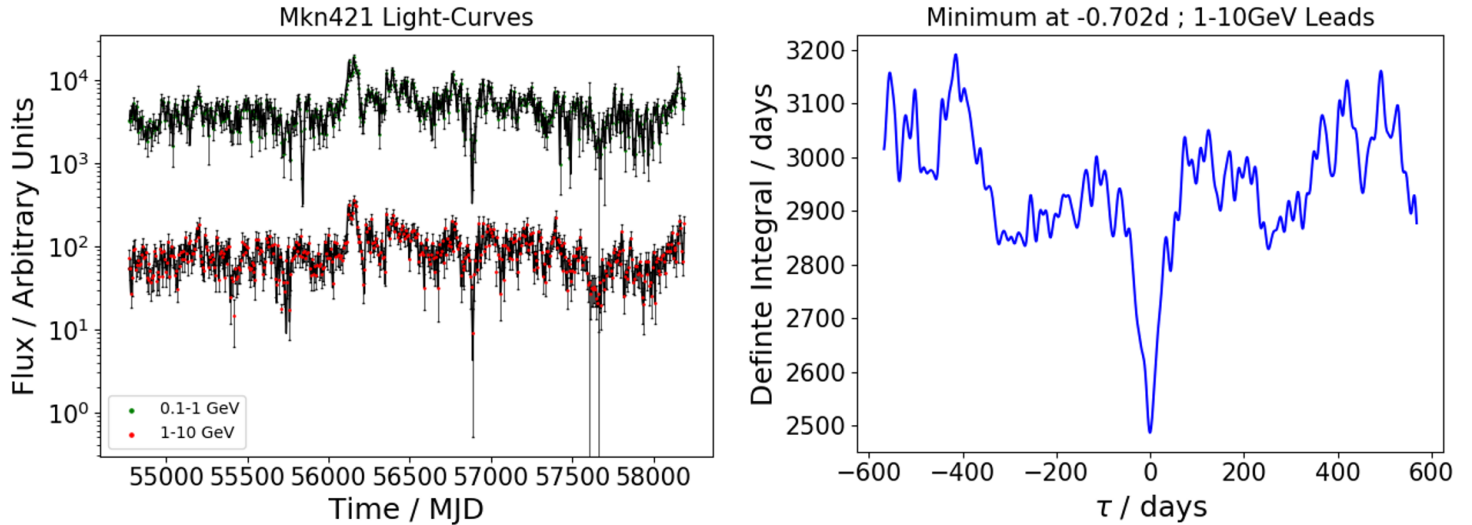


FIG. 10: Newly devised integral method for measuring τ . *Left:* Cubic interpolation yields a continuous function [black] over ~ 9.3 yr LCs, calculated in the energy range 0.1-1 GeV [green] and 1-10 GeV [red]. On visual inspection, perhaps high energy leads. *Right:* Results of calculating overlap integral (Eq. 7) show integral is minimised (2487 d as compared to t limits over 2274 d) at $\tau \sim -0.7$ d, implying a 1-10 GeV lead. The method is potentially viable, as evidenced by a smooth curve around $\tau = 0$; however, no error on τ has been calculated, function resolution is arbitrary, method relies on well-sampled, low variability LC inputs, and LC flux errors have been ignored. More work is required.

pairs/initial DCCFs in Appendix. G). Firstly on LCs, while it's unclear why blazar data is unanimously corrupted around ~ 58300 MJD (e.g. spurious on-board events, multiple coincident flares, GTI filtering failures), LC point absence in this region may effect lag results; in future, data beyond ~ 58300 MJD should be removed temporarily, and the resulting DCCF inspected and compared, to affirm false correlations were not introduced. Also, F1 gamma-ray LC was fastidiously constructed, correcting for bright periods by varying binsperdec (§3.3); LC comprises \sim half the number of data points as others (Table. III), which introduces a systematic difference into the pipeline. Although the root cause of model failures is correctly identified as an over-abundance of low-energy high-dispersion photons, *binned* likelihood analysis, whereby events are *not* treated individually, should be performed during bright flares/periods of outburst.

For DCCF analysis, lag (error) estimation is a non-trivial problem, and the validity of the bin-size error is based on a series of assumptions (§5.1). More rigorous methods (e.g. maximum likelihood estimations [101], model independent methods [102]), should be employed. E13 analysis demonstrates real LCs are poorly described by a Gaussian PDF. It is unclear then whether confidence intervals assuming Gaussian distributed probabilities are appropriate, which should be investigated. DCCF limited lag range may cut out significant (anti-)correlations: at $z = 0$, our maximum $|\tau| = 1350$ d corresponds to only ~ 1 pc, as compared with a maximal jet extent of \sim Mpc, equivalent to an extreme upper limit of 3 Myr. In practice, the maximum lag should likely be set at some variability time-scale subtracted from the LC length. Linear

de-trending of LCs could also be explored; by removing large time-scale (\sim year) variations, lag measurements on short time-scales (\lesssim month) may be improved [39, 96]. Conversely, short time-scale variability could be removed, and lags sought for only on the largest time-scales.

Continuing with this theme, in FSRQs, we note sparse periods of radio sampling (particularly F(3,4,5)), and/or a lack of intrinsic radio variability (as compared to gamma-rays e.g. F1), apparently leads to damping of significant DCCF peaks (Table. IV), despite the expectation following visual inspection, that the LC pair should be correlated on large time-scales. Crucially though, success rate tests tell us radio clustering and sparse sampling does not *necessarily* limit the potential for significant correlations to register in the DCCF. Yet in F(1,3,4,5) & B3[LBL], all peaks aligned with expectations are $<3\sigma$. Perhaps then, the assumption on which the success rate tests is based, that the LC pairs are coupled by a single unique time-lag, is falsified. Assuming with confidence the global correlation is real, either, there are a mix of lags that serve to damp out the DCCF peak, or, only a fraction of flares observed in the (more variable) gamma-ray LC are correlated with those of the radio, *despite* poor radio sampling (or a combination of both effects). We might conclude the static single-zone model does not hold; either there are multiple cores, single cores with time-variable separation, or there are multiple mechanisms at work that each account for/contribute towards short and long term variability²⁵.

On reflection though, the sampling locations relative to local LC activity is just as important as the global sampling/cluster profile, as evidenced by Fig. 11. Most likely, we are hampered by a combination of effects (chance radio sampling missing/capturing radio activity, intrinsic lack of variability/mix of lags), and so we can draw no firm conclusions on F(3,4,5) and B3.

F1 gamma-ray LC is poorly sampled, and double peak requires further inspection (Appendix. F). In F2, while it is clear the LCs are not correlated on large time-scales, short time-scale flares *are* correlated (Ref. [41] and references therein). F6 is consistent with a static single-zone model. Although B4[LBL] peak is significant, Fig. 7 demonstrates radio lead may be an artefact of chance radio sampling. Assuredly, IBL B5 LCs show no correlation, implying two discrete emission mechanisms. IBL B2 is particularly interesting, exhibiting a significant anti-correlation when LC time is limited to $t < 56800$ MJD (perhaps when cores are static). A mechanism whereby energy of a fixed budget is directly transferred between radio and gamma-ray cores has not yet been recorded in the literature. B1 and B6 are poorly sampled, highly clustered, low variability HBLs, with low success rates (excessively so in the case of B6). No firm conclusions can be drawn without more radio data, only that the well sampled gamma-ray LCs are also low variability, again implying a shared mechanism for global variability²⁶.

All blazars falling under the ‘~’ Conclusion (Table. IV) need further inspection on shorter time-scales. Save for B2, no effort has been made to analyse trims of the full 11-year time series. While global correlation is conclusively present/absent in all blazars (bar B1, B6), examination of flares on short time-scales, and contesting hypotheses of mixed lags versus radio

²⁵ Compare F3 and F6 for example. Despite sharing similar success rates, clustering, and radio sampling, F6 exhibits a significant peak, and F3 does not. This could be accounted for not by sampling, but by intrinsic differences - however, Fig. 11 demonstrates chance radio sampling could also be responsible.

²⁶ As will be discussed, in HBL gamma-ray LCs, we are sampling a relatively low flux region away from the SED peak (Fig. 3), which may bias our results.

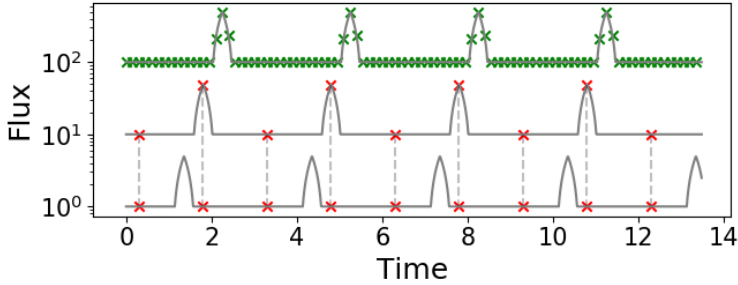


FIG. 11: Qualitative plot demonstrates that, for a unique radio sampling profile [red], correlation detection probability depends on the true radio offset from the gamma-ray LC [green].

flare absence, will be informative. LC re-binning for long term analysis should also be explored.

Scope for physical interpretation is limited. Ref. [103] cite independent root causes for long and short term variability as, central engine processes, and magnetic reconnection/jet-turbulence, respectively. Outliers B5 and F2 lack global correlation, implying mixed emission mechanisms can manifest universally, regardless of blazar sub-class. Recalling Fig. 3, our findings provide for a direct test of the radiative cooling model (§1.1). Including ‘~’ results, lags are predominantly gamma-ray leading correlations, mimicking literature findings (Table. I). LBLs B3/B4 (that reside closest to FSRQs) exhibit radio-leading correlations. These findings are consistent with radiative cooling: a burst of external seed photons incident on FSRQ jets would lead to shock-in-jet gamma-ray leading lags (upstream gamma-ray core); a burst of synchrotron photons in LBLs would be closely followed by gamma-ray emission. In bluer BL Lacs, it seems the causal disconnect widens. Adopting a spine-sheath model or needle-in-jet scenario, this could be due to inclination, given that emission would *not* dominate the entire jet cross-section.

Scope for future work is vast. On top of short time-scale flare studies (with potential for daily binned gamma-ray LCs), periodicities/QPOs which may manifest in our gamma-ray LCs (e.g. B2, B3, Appendix. F), should be explored. Spectral index/PSD evolution is also an interesting avenue; particularly, time lags manifesting in different spectral/LC states (e.g. hard vs soft, quiescence vs outbursts/flares) should be compared and contrasted. More generally, a wider sample size is needed to contrast FSRQs with BL Lacs. Moreover, a bias is placed implicitly on our observations, given a well defined energy range occupies a unique, target-specific portion of the SED (e.g. Figs. 1, 3). In future utilising a suite of radio (e.g. SCUBA-2 [850/450 μ m], OVRO [20mm], LOFAR [1-30m] etc.) and gamma-ray (e.g. VERITAS [0.25-1 TeV], CTA [\sim 0.1-300 TeV]) observatories will provide, not only for unbiased observations, but for a deeper survey of the blazar population as whole, thereby picking out lower mass blazars, and directly testing the model of radiative cooling (§1.1, Appendix. A).

7. CONCLUSIONS

Understanding the as yet unknown blazar emission mechanisms, locations, and key governing parameters that give rise to the blazar sub-classes, is a continued effort in modern astrophysics (§1). This investigation constructs, and performs correlation analysis on, weekly-binned gamma-ray and irregularly sampled radio light curves of 12 bright and variable blazars, from 11 years of *Fermi*-LAT and SMA data. Limiting our analysis to the full time-series, sparse radio sampling is a critically limiting factor, that acts both to excite false positive DCCF peaks, and to damp true peaks owing to global LC coupling. On accepting/discardng raw DCCF results, LC

visual inspection, and colour maps of significant contributing LC points, are most informative. Success rate tests, and consideration of radio sampling, clustering, and consistency with the null hypothesis, are also considered to make informed decisions. Areas for improvement in the LC construction/DCCF analysis methods are detailed in §6.

Limited results yield only a handful of firm conclusions. Lags of the order ~ 10 d, corresponding to gamma-ray/radio core separations $\sim 1\text{-}10$ pc, are found. Findings indicate loose consistency with the radiative cooling model: FSRQs predominantly exhibit correlated gamma-ray leads, consistent with the shock-in-jet scenario, whereas LBLs exhibit radio-leads, implying bursts of low energy synchrotron seeds induce high-energy activity. No correlation with black hole mass is evident. Split-band LCs imply a shared emission location in the gamma-rays, and a new method is devised, with the potential to yield high temporal resolution from weekly-binned LCs. F6 is the only example that is consistent with a static single-zone model. Time-limited B2 LCs exhibit a highly significant ($>8.38\sigma$) anti-correlation, which is not readily explained by any of the popular needle-in-jet, spine-sheath, multi-zone models etc. Future work must evaluate correlations of well-sampled regions on small time-scales (and blazar-specific energies), so as to contest multi and single-zone models, and disentangle long and short term coupling (which, owing to analysis of F2/B5, appears to be independent of sub-class). Exciting leads for future work (§6), coupled with new VHE observations, will help both to elucidate the emission mechanisms in blazars, and to uncover the wider, more diverse population of low mass blazars.

ACKNOWLEDGMENTS

Many thanks to Paula and Anthony for all your support and guidance during our fantastically entertaining weekly meetings; I've had a really great time this year. Thanks also to Atreya for our rich discussions on Fermitools, to Max and Jasmine for their efforts on the fermipy tutorials, and to Tom for his invaluable tips on wielding the E13 software. Best wishes to everyone in the gamma-ray department, and I look forward to crossing paths soon!

REFERENCES

- [1] Lynden-Bell D., 1969, *Nature*, 223, 690
- [2] Garcia J., et al., 2019, *BAAS*, 51, 284
- [3] Reynolds C. S., 2019, *Nature Astronomy*, 3, 41
- [4] Dressler, A. & Gunn, J. E. 1983, *ApJ*, 270, 7
- [5] Dressler, A., et al. 1999, *ApJS*, 122, 51
- [6] Kellermann, K. I., et al. 1989, *AJ*, 98, 1195
- [7] Ghisellini, G., 2016, *Galaxies*, 4, 4, 36
- [8] Urry, C. M., & Padovani, P., 1995, *PASP*, 107, 803
- [9] Urry, M., 2003, *ASPC*, 290, 3
- [10] Blandford, R., et al. 2018, *Annual Reviews*, 57, 467
- [11] The Fermi-LAT Collab., 2019, arXiv:1902.10045
- [12] Sbarrato T., et al. 2014, *MNRAS*, 445, 81
- [13] Kellermann, K. I., et al. 2004, *ApJ*, 609, 539
- [14] Boula, S., et al. 2019, *Galaxies*, 7, 1, 3
- [15] Aharonian, F., et al. 2007, *ApJ*, 664, 71
- [16] Raiteri, C. M., et al. 2013, *MNRAS*, 436, 1530
- [17] Raiteri, C. M., et al. 2017, *Nature*, 552, 374
- [18] Shah, Z., et al. 2019, *MNRAS*, 484, 3168
- [19] Penrose, R., et al. 1971, *Nature*, 229, 177
- [20] Blandford, R. D. & Znajek, R.L., 1977, *MNRAS*, 179, 133
- [21] Blandford R.D., Payne D.G., 1982, *MNRAS*, 199, 883
- [22] Fabian, A. C., 2012, *A&A*, 50, 455

- [23] Bambic, C. J., Reynolds, C. S., 2019, ApJ, 886, 78
- [24] Verscharen, D., et al. 2019, arXiv:1908.02206
- [25] Urry, C.M., & Padovani, P., 1995 PASP, 107, 803
- [26] Madejski, G., & Sikora, M., 2016, ARAA, 54, 725
- [27] Mannheim, K., et al. 1992, A&A, 253, 21
- [28] Liodakis, I., et al. 2018, MNRAS, 480, 4, 5517
- [29] Maraschi, L., et al. 1992, ApJ, 397, L5
- [30] Dermer, C. D., et al. 1992, A&A, 256, 27
- [31] Dermer, C. D., et al. 1993, ApJ, 416, 458
- [32] Sikora, M., 1994, ApJ, 421, 153
- [33] Kataoka, J., et al. 1999, ApJ, 514, 138
- [34] Abdo, A. A., 2010a, ApJ, 716, 30
- [35] Ghisellini, G., et al. 2017, MNRAS, 469, 1, 255
- [36] Fossati, G., et al. 1998, MNRAS, 299, 433
- [37] Furhmann, L., et al. 2014, MNRAS, 441, 1899
- [38] Max-Moerbeck, W., et al. 2014, MNRAS, 445, 1
- [39] Ramakrishnan, V., et al. 2015, MNRAS, 452, 1280
- [40] Ramakrishnan, V., et al. 2016, MNRAS, 456, 171
- [41] Prince, R., 2020, ApJ, 890, 164
- [42] Alston, W. N., et al. 2020, Nature Astron., 2A
- [43] Kara, E., et al. 2019, Nature 565, 198
- [44] Marscher A. P., Gear W. K., 1985, ApJ, 298, 114
- [45] Turler M., 2011, Mem. d. Soc. Ast. Italiana, 82, 104
- [46] Lobanov, A., 2010, arXiv:1010.2856
- [47] Bonnoli G., et al. 2011, MNRAS, 410, 368
- [48] Ghisellini, G., et al. 2008, MNRAS, 386, 28
- [49] MacDonald, N. R., et al. 2015, ApJ, 804, 111
- [50] Rachen, J. P., et al. 2010, arXiv:1006.5364
- [51] Marscher, A. P., 2013, arXiv:1304.2064
- [52] <http://teacherlink.ed.usu.edu/tlnasa>
- [53] Arkhangelskaja, I.V. , et al. 2015, Moscow Conf.
- [54] Blackett, P. M. S., Dec 13th 1948, Nobel Lecture
- [55] Atwood, W. B., et al. 2009, ApJ, 697, 1071
- [56] Ackermann, M., et al. 2012, ApJ, 203, 4
- [57] Greisen, K, 1966, Physics Review Letters, 16, 748
- [58] Zatsepin, G. T., Kuz'min, V. A., JETPL, 4, 78
- [59] Bird, D. J., et al. 1995, ApJ, 441, 144
- [60] Neyman, J., et al. 1928, Biometrika, 20A, 175
- [61] Mattox, J. R., et al. 1996, ApJ, 461, 396
- [62] Wilks, S. S., 1938, Ann. Math. Stat., 9, 60
- [63] Abdo, A. A., et al. 2009, ApJ, 183, 46
- [64] Hovatta, T., et al. 2008, A&A, 485, 51
- [65] Hervet, O., et al. 2017, A&A, 592, 22
- [66] Ryan, J. L., et al. 2019, arXiv:1909.04227
- [67] Ghisellini, G., et al. 2009b, MNRAS, 399, 2041
- [68] Xiong, D. R., et al. 2014, MNRAS, 441, 3375
- [69] Krauss, F., et al. 2016, A&A, 591, A130
- [70] Gupta, A. C., et al. 2017, MNRAS, 472, 788
- [71] Sbarato, T., et al. 2012, MNRAS, 421, 1764
- [72] Gu M., et al. 2001, MNRAS, 327, 1111
- [73] Abdo, A. A., et al. 2010b, ApJ, 710, 810
- [74] Fromm, C. M., et al. 2015, A&A, 576, A43
- [75] Shukla, A., et al. 2018, ApJ, 854, 26
- [76] Wagner, R. M., 2008, MNRAS, 385, 119
- [77] Agarwal, A., et al. 2016, MNRAS, 455, 680
- [78] Tanaka, Y. T., et al. 2013, ApJ, 777, 18
- [79] Ghisellini, G., et al. 2011, MNRAS, 414, 3, 2674
- [80] Abdu, M. A., et al. 2005, JASTP, 67, 1643
- [81] Ghisellini, G., et al. 2014, Nature, 515, 376
- [82] Hughes, I.G., Hase, T.P.A, 2010, OUP, Oxford, UK
- [83] P. T. Ho, et al. 2004., ApJ, 616, 1
- [84] Blundell, R., 2007, IMS Digest, 1857
- [85] Fomalont, E., et al. 2014, The Messenger, 155, 19
- [86] Matsushita, S., et al. 2006, PSISOE, 6275, 62751
- [87] Gurnwell, M. A., 2009, SMA Science Symposium 2009
- [88] Nikolic, B., et al. 2008, The Messenger, 131, 14
- [89] Gurnwell, M. A., et al. 2007, ASP Conf. Series, 375, 2007
- [90] Nikolic, B., 2013, A&A, 552, 104
- [91] Algaba, J. C., et al. 2018, ApJ, 852, 30
- [92] Strom, A., 2009, Fermi Symposium, arXiv:1001.0806v1
- [93] Krips, M., et al. 2018, arXiv:0710.4956
- [94] Edelson R. A., Krolik J. H., 1988, ApJ, 333, 646
- [95] Lee Rodgers, J., & Nicewander, W. A., 1988, AmSci, 42, 59.
- [96] Welsh W. F., 1999, PASP, 111, 1347
- [97] Jones, E., et al. 2001, <http://www.scipy.org/>
- [98] Timmer, J., Koenig, M., 1995, A&A, 200, 707
- [99] Emmanoulopoulos, D., et al. 2013, MNRAS, 433, 907
- [100] Connolly, S. D., 2016, ASCL, 1602.012
- [101] Alexander, T., 2013, arXiv:1302.1508
- [102] Peterson B. M., et al. 1998, PASP, 110, 660
- [103] Zhang, H. M., et al. 2020, arXiv:2003.11175
- [104] Giommi, P., et al. 2012, MNRAS, 420, 2899
- [105] Boone, F., 2001, A&A, 377, 368
- [106] Keto, E., 1997, ApJ, 475, 843

Appendix A GAMMA-RAY CORE LOCATION

A gamma-ray core ‘close’ to the SMBH (on sub-pc down to $\sim 100R_g$ scales, $R_g = \frac{GM_{BH}}{c^2}$) is favoured by multiple, independent observational findings. These are summarised in Refs. [37, 41, 65] as: rapid (\leq hour) gamma-ray variability coupled with the assumption the gamma-ray core emission dominates the jet cross section, high-energy spectral breaks due to BLR pair production opacity, and observational consistency with SED models employing disk/BLR-ERC scenarios. Conversely, multi-wavelength temporal-correlation studies successfully tie high-energy wavebands (gamma-ray, X-ray, optical) to radio-shock features propagating outwards on length scales \gtrsim pc, measured directly using Very Long Baseline Interferometry techniques. Additionally, BLR pair-production opacity does not permit the very-high-energy (\sim TeV) variability observed on \sim minute time-scales.

Appendix B FERMI-LAT BACKSPLASH EFFECT, READOUT & EVENT PROCESSING

The segmentation of the ACD is included to combat the ‘backsplash effect’²⁷, whereby secondary particles in the LAT (most often 0.1-1 GeV photons) move up the TKR, to Compton scatter in the ACD. This can result in the issuing of a veto signal coincident with the arrival of a source gamma-ray; i.e. desirable photon detections are discounted due to ‘self-veto’. ACD segmentation ensures only tiles in the near vicinity of the incident secondary particle will experience self-veto, thereby reducing the area that contributes to backsplash.

To initiate readout of a potential gamma-ray interaction, signals (or ‘trigger primitives’) from LAT components (ACD, TKR, CAL) are collated by the Central Trigger Unit; a global trigger for event readout is issued if a trigger condition is satisfied. As mentioned in §2.1, the ACD can issue a veto signal, which prevents readout. The TKR trigger primitive is described in Fig. 2. Finally, CAL modules can issue two trigger primitives, signalling the detection of an event above a low energy (100 MeV) and high energy threshold (1 GeV). While the former is not necessarily required for readout, the latter prevents readout in the case of most low energy γ -ray events (Engine 7), but is instead required for detection of high energy photons (Engine 6). More details on these trigger conditions are described in Ref. [56].

Global readout begins ‘Level 0 processing’, the end products of which are Level 0 data packets, stored in the on-board Solid State Receiver (SSR). Raw background flux creates an average global trigger rate of ~ 1.5 kHz, which is reduced by on-board filtering to ~ 400 Hz, which in turn typically comprises only $\sim 2\text{-}5$ desirable source photons. This on-board processing is performed by the Data Acquisition System (DAQ). As mentioned, the DAQ minimises the acceptance of CR interactions and other background sources, and maximises the acceptance of true source gamma-rays [55].

DAQ processing is governed by Pass 8 software, which has been updated three times from the

²⁷ The backsplash effect is a trait of the high mass Calorimeter: ~ 1800 kg. The Calorimeter is designed to be highly-absorbing, so as to mitigate energy losses, and has a thickness equivalent to 8.6 radiation lengths at normal incidence. This means secondary particles are prone to scattering back up the TKRs.

```

data:
  evfile : events.txt
  scfle : spacecraft.fits

  binning:
    roiwidth : 15.0
    binsz : 0.1
    binsperdec : 10

  selection:
    emin : 100
    emax : 10000
    zmax : 90
    evclass : 128
    evtype : 3
    tmin : 246823875
    tmax : 362560995
    filter : (DATA_QUAL>0)&&(LAT_CONFIG==1)&&(ABS(ROCK_ANGLE)<52)
    roicut : 'no'
    target : '4FGL J2253.9+1609'

  gtlike:
    edisp : True
    irfs : 'P8R3_SOURCE_V2'
    edisp_disable : ['isodiff', 'galdiff']

  model:
    src_roiwidth : 25.0
    galdiff : '$FERMI_DIFFUSE_DIR/gll_iem_v07.fits'
    isodiff : 'iso_P8R3_SOURCE_V2_v1.txt'
    catalogs : 'gll_psc_v20.xml'

```

FIG. 12: A typical config.yaml file.

initial Pass 6 software at launch²⁸. SSR data packets are transmitted to the ground, at an average rate of $\sim 1.2 \text{ MBs}^{-1}$, for processing into Level 1 Data. This ground analysis involves event reconstruction using pattern recognition and fitting algorithms, so as to distinguish between true source gamma-rays interactions, and those due to background sources [56]. Level 1 processing also determines $(E'_\gamma, \hat{p}'_\gamma)$, the inferred photon energy and direction of incidence, respectively. As mentioned, the background rate is reduced by a net factor of 10^6 , and retention of true source gamma-ray events is $\sim 75\%$ [55]. Atwood et al. (2009) also discusses false positive events, i.e. background interactions that appear as astrophysical gamma-rays; these are not significant [55].

Appendix C RESIDUAL MAP SOLUTIONS

The binsperdec parameter is set in the config.yaml file, a typical example of which is shown in Fig. 12. Fig. 6 showcases the over-fitting solution, of lowering and optimising the binsperdec parameter. By loading in the edisp_P8R3_SOURCE_V2_EDISP.fits file, the energy dispersion function, $D(E)$, is calculated following the prescription below. For more details, see²⁹. Gaining access to residual map pixel values is non-trivial, requiring manipulation of WcsNDMaps; instead, the natural gta.residmap() plot outputs are visually inspected, and compared for a range of binsperdec values, as in Fig. 6.

²⁸ Pass 8 primarily targets and mitigates the effects of ‘ghost events’, which are remnant electronic signals from discounted trigger events, that appear in the readout of accepted trigger events. Further improvements with Pass 8 software are detailed here: https://fermi.gsfc.nasa.gov/ssc/data/analysis/documentation/Cicerone/Cicerone_Data/LAT_DP.html

²⁹ https://fermi.gsfc.nasa.gov/ssc/data/analysis/documentation/Cicerone/Cicerone_LAT_IRFs/IRF_E-dispersion.html

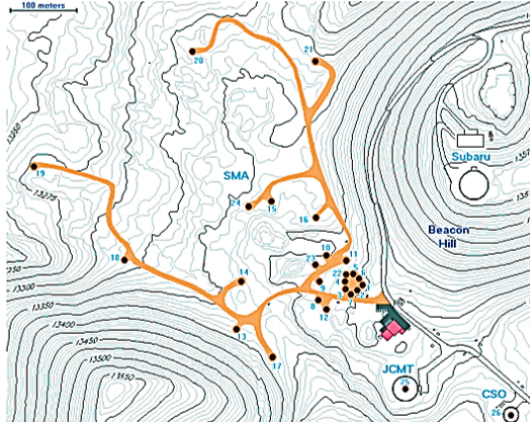


FIG. 13: Image is taken from Ho, Moran & Lo, 2004 [83], and depicts the SMA layout of 24 array pads, which yield 4 optimised Realeaux triangles, each contributing a different angular resolution. Each nested ring comprises at most 8 pads, and thus the cost of 8 pads is saved by sharing pads between rings. When required, a telescope (of mass $\gtrsim 5 \times 10^4$ kg) is moved via a specially designed transporter.

$$\frac{\delta E}{E} = \frac{E' - E}{E} \quad ; \quad x = \frac{\delta E}{E \cdot S_D(E, \theta)} \quad (8)$$

$$S_D(E, \theta) = c_0(\log E)^2 + c_1(\cos \theta)^2 + c_2(\log E) + c_3(\cos \theta) + c_4 \log E \cos \theta + c_5 \quad (9)$$

$$g(x; \sigma, k, b, p) = \frac{p}{\sigma \Gamma(1/p)} \frac{k}{1 + k^2} \begin{cases} \exp(-\frac{k^p}{\sigma^p} |x - b|^p), & \text{if } x - b \geq 0. \\ \exp(-\frac{1}{k^p \sigma^p} |x - b|^p), & \text{if } x - b < 0. \end{cases} \quad (10)$$

$$D(x) = F \times g(x; \sigma_1, k_1, b_1, p_1) + (1 - F) \times g(x; \sigma_2, k_2, b_2, p_2) \quad (11)$$

Appendix D SMA ARRAY DESIGN

The underlying principle of an interferometer is to improve the diffraction limited angular resolution of a single antenna ($\theta \sim \frac{\lambda}{D}$) by observing with multiple antennae, thereby creating a large effective baseline, D_b , thus $\theta \sim \frac{\lambda}{D_b}$. In the simplest interferometer configuration (2 antennae), the effective baseline is the antenna separation, $D_s = D_b$; however, solving for the optimal configuration of multiple antennae, that maximises D_b , is a formidable problem; direct trial and error methods evaluate image quality based off some pre-selected configuration (e.g. Y-shape, T-shape, triangle, circle etc.), but do not guarantee that the optimal configuration has been found, whereas inverse methods, that attempt to derive the array configuration from high quality image specifications, require complex algorithms to solve for this ultimately ill-posed problem [105].

The relative locations of the antennae are an important feature, that governs the sampling of the so-called ‘ $u - v$ plane’. As described in Ref. [83], image quality is optimised for the SMA

by sampling the $u - v$ plane uniformly in a circular boundary. The array design is a Reuleaux triangle (as in Fig. 13), whereby 3 points (forming an equilateral triangle) are connected by curved lines, along which antenna sitting-locations or ‘pads’ are placed. This configuration was optimised with neural network algorithms [106], for a ‘small’ number of elements (i.e. 8 elements here as opposed to e.g. Y-shape VLA comprised of 28 elements³⁰). The array design maximises angles between baseline vectors, which in turn optimises the uniformity of sampling in the $u - v$ plane, and so the image quality.

A single movable antenna has a primary parabolic reflecting dish surface comprised of 4 layers, each with 72 machined cast aluminium panels, and a surface accuracy of $12\mu\text{m}$, optimised from $60\mu\text{m}$ following holographic testing [83, 84]. Radio waves are focussed by the primary reflector onto the machined cast aluminium secondary reflector, which in turn directs waves towards the receiver; details of the subsequent electronic and data processing, calibration procedures, and corrections for e.g. dish deformation due to gravity, are discussed further in Refs. [83, 84, 86].

Appendix E SUCCESS RATE PRESCRIPTION

Total, correlated, anti-correlated and un-correlated success rates are calculated. For example, the probability that the LCs are truly correlated, given the DCCF peak appears correlated, $P(\text{True_C}|\text{App_C})$, is calculated with Bayes’ Theorem:

$$P(\text{True_C}|\text{App_C}) = P(\text{App_C}|\text{True_C}) \frac{P(\text{True_C})}{P(\text{App_C})}. \quad (12)$$

$P(\text{App_C}|\text{True_C})$ is calculated as the number of successes over the number of simulations, correlating the real gamma-ray LC with the fake radio LC (constructed as described in §5.1). $P(\text{True_C})$ is $\sim 1/3$, where fake LC is equally distributed as being truly correlated (C), anti-correlated (AC) and ‘un-correlated’ (UC). $P(\text{App_C})$ is thus calculated as,

$$\begin{aligned} P(\text{App_C}) &= P(\text{App_C}|\text{True_C})P(\text{True_C}) + P(\text{App_C}|\text{True_AC})P(\text{True_AC}) \\ &\quad + P(\text{App_C}|\text{True_UC})P(\text{True_UC}). \end{aligned} \quad (13)$$

Truly anti-correlated LCs, LC_{AC} , are constructed using LC_C , the truly correlated fake radio LCs. $LC_{AC} = 2 \cdot \max(LC_C) - LC_C$. Un-correlated LCs are created using TK95.

Appendix F TARGET NOTES

These notes detail initial DCCF results, and choices made to accept/discard/search for new DCCF peaks. Tools employed include DCCF confidence intervals (§5.2), success rates (Table. 9), consideration of LC sampling and radio clustering (Table. 14), consistency with the null hypothesis (Table. 14), visual inspection (§5.2, Appendix. G), and colour plots mapping UCCF

³⁰ <https://public.nrao.edu/telescopes/VLA/>

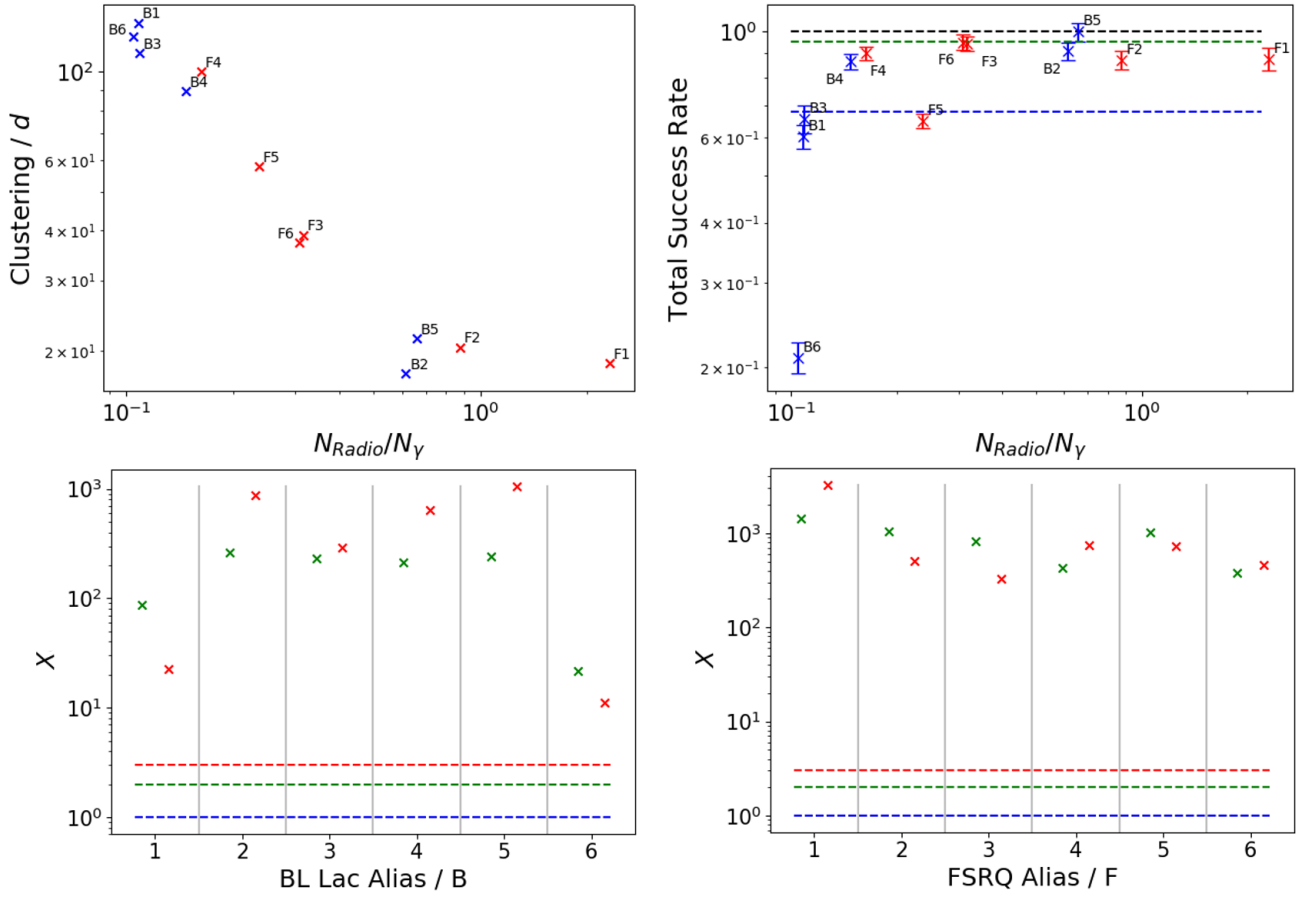


FIG. 14: *Upper Left:* Plot shows SMA radio LC ‘clustering’ against relative radio/gamma-ray sampling, $N_{\text{Radio}}/N_\gamma$ (number of radio LC points divided by number of gamma-ray points). Clustering is defined as the standard deviation of LC data point time separations (clustering=0 implies evenly sampled light curve, high clustering implies LC comprised of closely and widely spaced points). The downwards trend is unsurprising following a visual inspection of LCs, and either parameter can be used as a proxy for the other. *Upper Right:* Plot shows total success rate (Table. 9) against radio sampling. Plot suggests the lower the radio sampling, the lower the success rate. (68,95,100)% colour lines plotted [blue, green, black]. *Lower Panels:* Results of investigation into LC consistency with the null hypothesis (a constant flux) are shown [38]. Defining $\sigma = \sqrt{2\nu}$ [82], $\chi^2_{\min} = \nu + X\sigma$, $X=(1,2,3)$ dashed lines plotted [blue, green, red]. All gamma-ray [green marker] and radio [red marker] LCs are inconsistent with observational noise, and variability is due, at least in part, to true intrinsic variability. Interestingly, B6 which resides closest to the null hypothesis has the lowest success rate, and the lowest radio sampling. Similarly, B1, with the most clustering, has a low success rate, and a radio LC close the the null hypothesis.

points to the LCs (Figs. 8, 16, 17). Peak significances are quoted with upper and lower uncertainties, resolved by DCCF points obtained from 10,000 E13 synthetic LCs [99]; maximum fake DCCF points typically occurs at $\sim 8.38\sigma$. Where real DCCF exceeds this height, measurement is written as a lower limit.

(F1) 3C 454.3: DCCF exclusively comprises a single broad peak ($>3\sigma$), which is maxi-

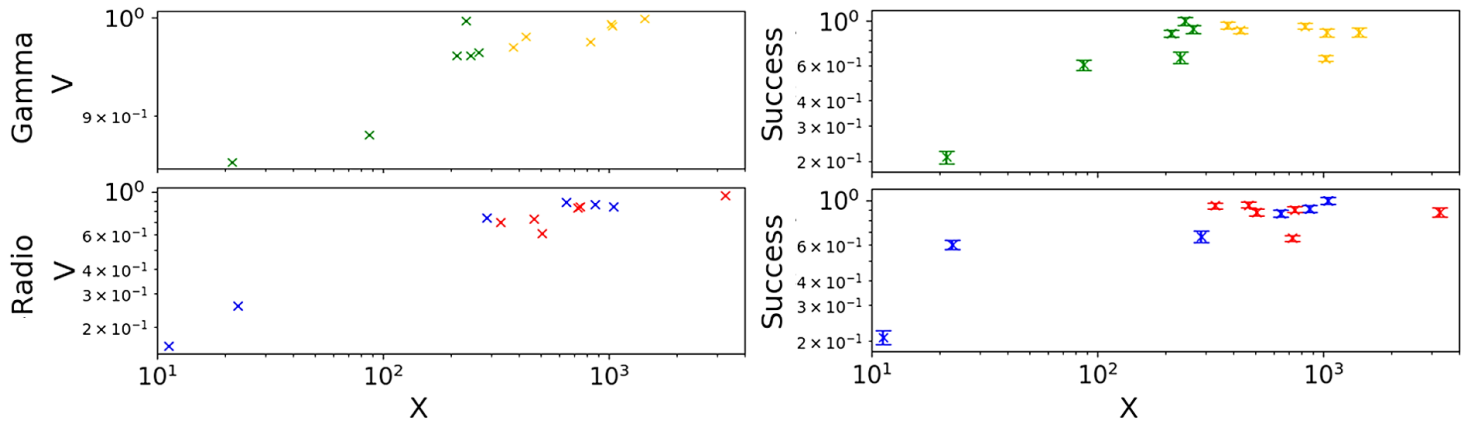


FIG. 15: For completeness; *Left*: Coupling of radio/gamma-ray variability indices, V , and inconsistency with the null hypothesis, X . *Right*: Total Success Rate dependence on X . BL Lacs [Gamma-Ray = green, Radio = blue], FSRQs [Gamma-Ray = orange, Radio = red].

mally anti-correlated ($>8.38\sigma$) at ~ 600 d. Colour plots reveal anti-correlation is fake (more in main text §5.2, Fig. 8), and a pair of correlated peaks of the order 10's of days (significances $2.31^{+0.07}_{-0.05}\sigma$, $2.29^{+0.06}_{-0.03}\sigma$) are selected for further inspection. Fig. 16 demonstrates colour maps do not aid in selecting one lag over the other. F1 is unique in having a 100% correlated success rate. This is, however, irrelevant, as we have ‘identified’ F1 as anti-correlated, which holds an associated success rate $73\pm 26\%$. Having disclaimed the anti-correlation, we claim F1 is correlated, with a low precision lag measurement, quoted as -16 ± 47 d.

(F2) 3C 279: DCCF shows only 1 significant peak ($3.11^{+0.25}_{-0.11}\sigma$) that is anti-correlated at -234 ± 8 d. LCs do not appear anti-correlated, colour maps are unconvincing, and anti-correlated success rate is $72\pm 7\%$. This peak is discarded, and we claim there is no anti-correlation.

(F3) PKS 1510-089: No significant peak is found, and the maximum at $2.52^{+0.15}_{-0.07}\sigma$ is a correlation at 28 ± 11 d; this is perhaps consistent with LC expectations. Un-correlated success rate is $87\pm 2\%$. Colour maps are somewhat convincing, however, broadly speaking, it seems only a number of flares in the radio are correlated with those in the gamma-ray, and the gamma-ray features many more flares. This may be a consequence of the radio sampling. This blazar needs further inspection on much shorter time-scales.

(F4) PKS 1502+106: Only a maximum at $1.85^{+0.08}_{-0.04}\sigma$ is found; similar to F3, this correlation is aligned with LC expectations, at a lag 84 ± 52 d. Colour maps are convincing, and this lag is likely. Low significance is accounted for by the lack of radio data, that means significant LC data that would contribute to the lag bin is missing, and mean/standard deviation is poorly characterised. This blazar also needs further inspection.

(F5) CTA 102: No significant peak is found, only a maximum correlated peak at a lag 55 ± 15 d, significance $2.27^{+0.13}_{-0.05}\sigma$, aligned with expectations following LC inspection. 3-prong structure is apparent (§5.2), and central peak is the maximum. Colour maps showing all contributing $|UCCF| > |DCCF|$ LC points are convincing. Low significance is likely a feature of mixed lags, as well as low radio sampling.

(F6) 4C+38.41: The single broad, significant ($>8.38\sigma$), and correlated peak centred around

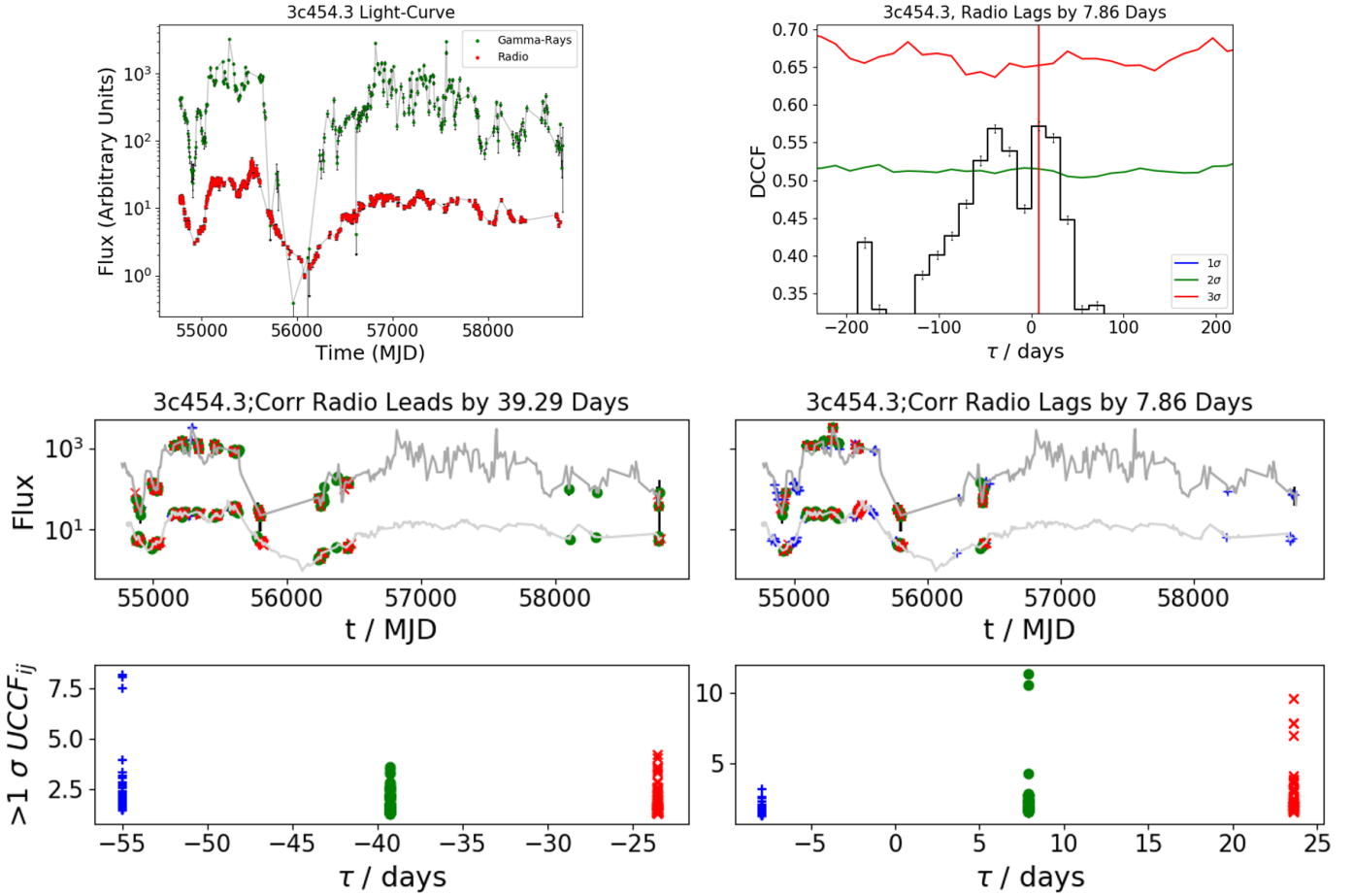


FIG. 16: Plots demonstrate preference cannot be lent to a radio lead or lag based off of colour maps in 3C 454.3. *Upper Left:* 3C 454.3 11-year light curve pair. *Upper Right:* DCCF showcasing two peaks ($>2\sigma$) that align with expectations derived from light curve inspection. *Lower Panels:* Colour maps trace UCCF points ($>1\sigma$) back to LCs, and both positive and negative lags map to the same points. Colour maps offer no evidence to prefer one lag over the other.

~ 25 d is precisely aligned with expectations following LC inspection. Correlated success rate is high at $97 \pm 2\%$. Contributing LC points from $|UCCF| > |DCCF|$ colour maps are well distributed. We can confidently claim there is a significant correlation, and quote a lag at 23 ± 13 d.

(B1) Mkn 421: Significant ($3.28^{+5.56}_{-0.46} \sigma$) anti-correlated peak at $\tau = -1301 \pm 34$ d is questioned, given an anti-correlation success rate of only $48 \pm 7\%$, the highest level of clustering, and a low relative radio sampling. On visual inspection of colour maps ($UCCF < DCCF$), the anti-correlation is unconvincing, with 1 of 2 radio cluster regions consistent with a null hypothesis ($\chi^2_\nu = (3.7, 1.04)$, respectively). By inspection of LCs, there is no obvious trend, owing to the lack of radio points. More radio data is required to confidently claim there is no (anti-)correlation.

(B2) S5 0716+71: Initial 11-year DCCF has no significant correlation, with a maximum anti-correlation at -18 d of $2.37^{+0.22}_{-0.12} \sigma$. LC pair shows no obvious trend. On visual inspection of

colour maps, the anti-correlation appears prominent at early times, and DCCFs are recalculated for $t < 56800$ MJD, yielding a peak $>8.38\sigma$ at -20 ± 6 d. DCCF features multiple $>3\sigma$ positive and negative peaks for $t > 56800$ MJD, and is not considered further.

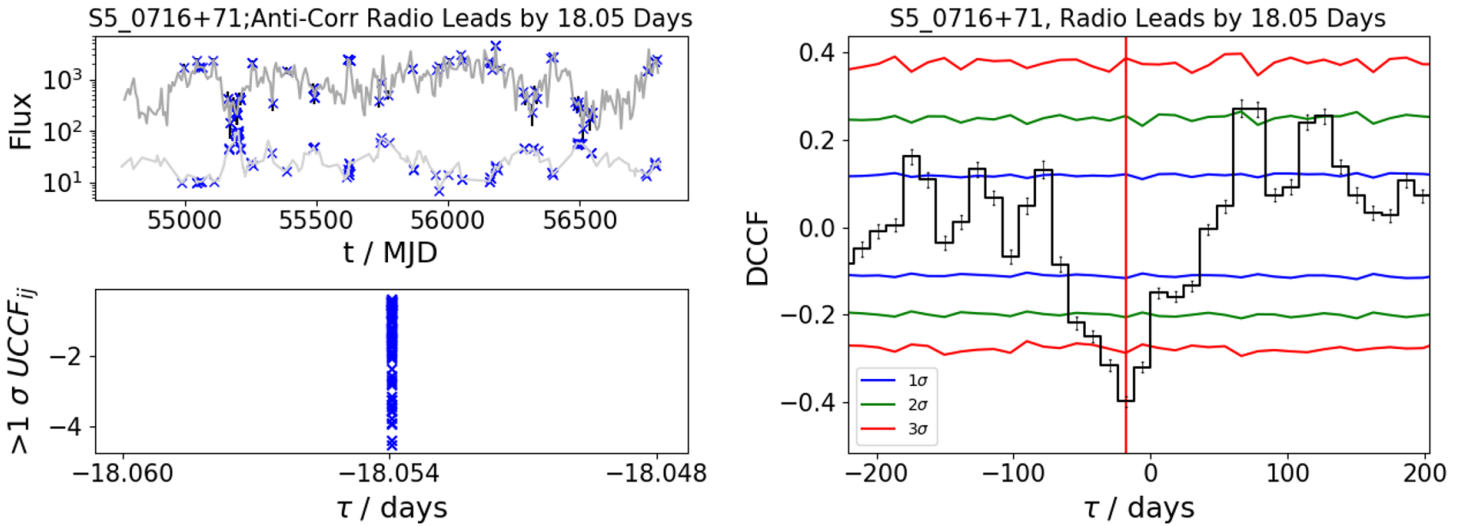


FIG. 17: B2 anti-correlation between LCs limited to $t < 56800$ MJD is compelling.

(B3) PKS 0426-380: Initial DCCF comprises 6 and 8 positive and negative significant peaks respectively, the most prominent of which (-738 d correlation at $>8.38\sigma$) is immediately discarded with the use of colour maps, revealing multiple correlations with regions consistent with the null hypothesis. Moreover, LCs appear over the full 11-year time-span to be correlated at a lag of the order ~ 10 's of days. A $2.62^{+0.32}_{-0.13}\sigma$ correlated peak at -57 ± 35 d is consistent with expectations, but the low radio sampling ultimately limits our capacity to claim confidence in this lag; more radio data is required.

(B4) PKS 0537-441: 4 significant correlations are found, the maximum of which at $3.25^{+0.45}_{-0.2}\sigma$ appears at a lag, -60 ± 51 d, aligned with expectations following visual inspection of LC pair. Although success rate is moderate, radio sampling is poor, casting doubt on the lag measurement. Colour plots show radio is well sampled during flare onset/rising, but there are no observations during flare decays, Fig. 7. Without radio data to act as a ‘buffer’ on the decaying side of flares, a bias is lent towards a radio lead. While the correlation is accepted, the lag is uncertain, and the large Gaussian standard deviation is applied as the lag uncertainty, -60 ± 117 d.

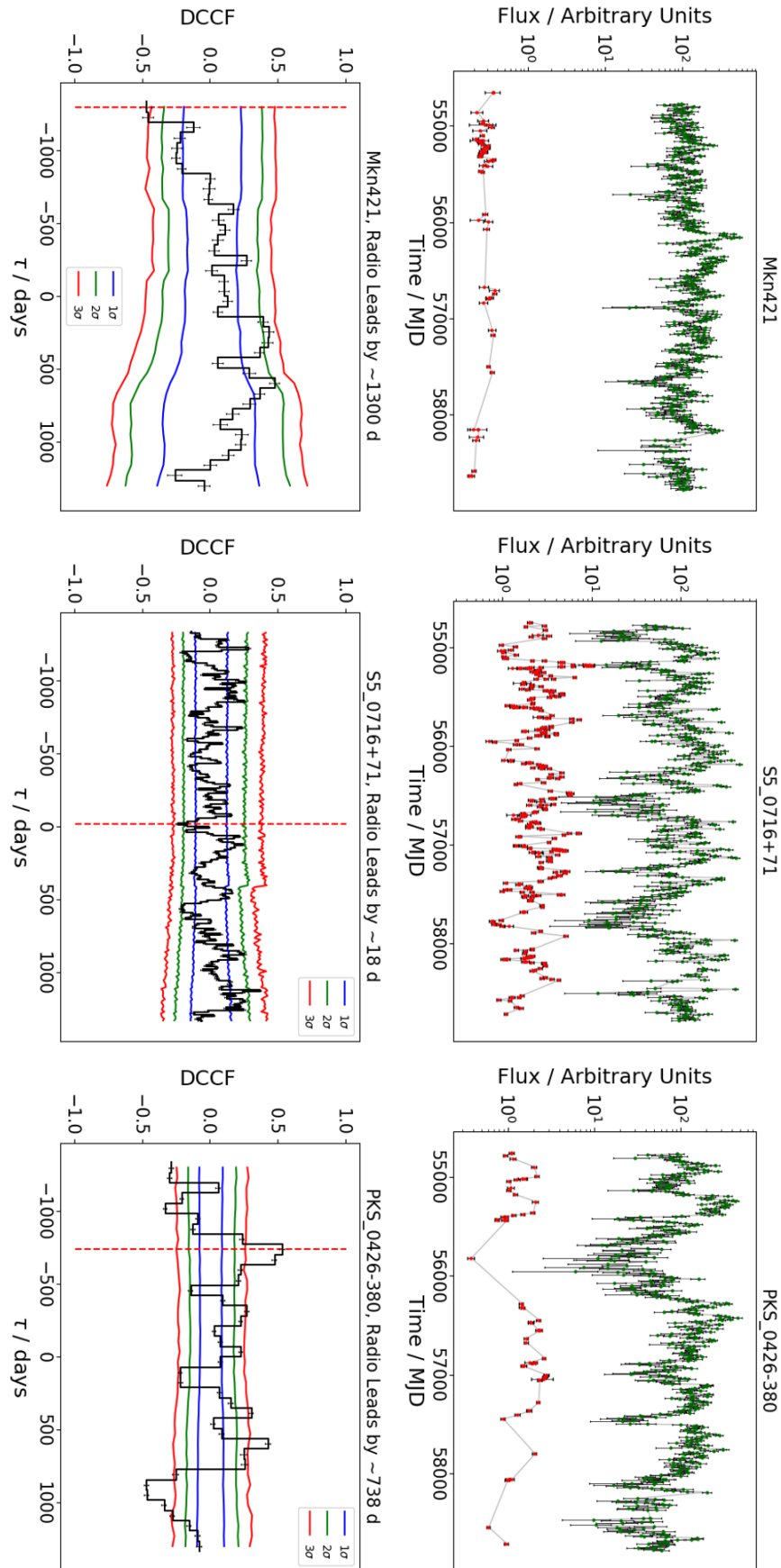
(B5) BL Lacertae: Maximum significance peak is anti-correlated at $1.91^{+0.16}_{-0.08}\sigma$. LCs and colour plots show no indication of a strong correlation or anti-correlation. Given the high success rate for un-correlated LCs in B5, $>99.2\%$, and good radio sampling (~ 0.66), we can confidently claim BL Lacertae exhibits no significant (anti-)correlation.

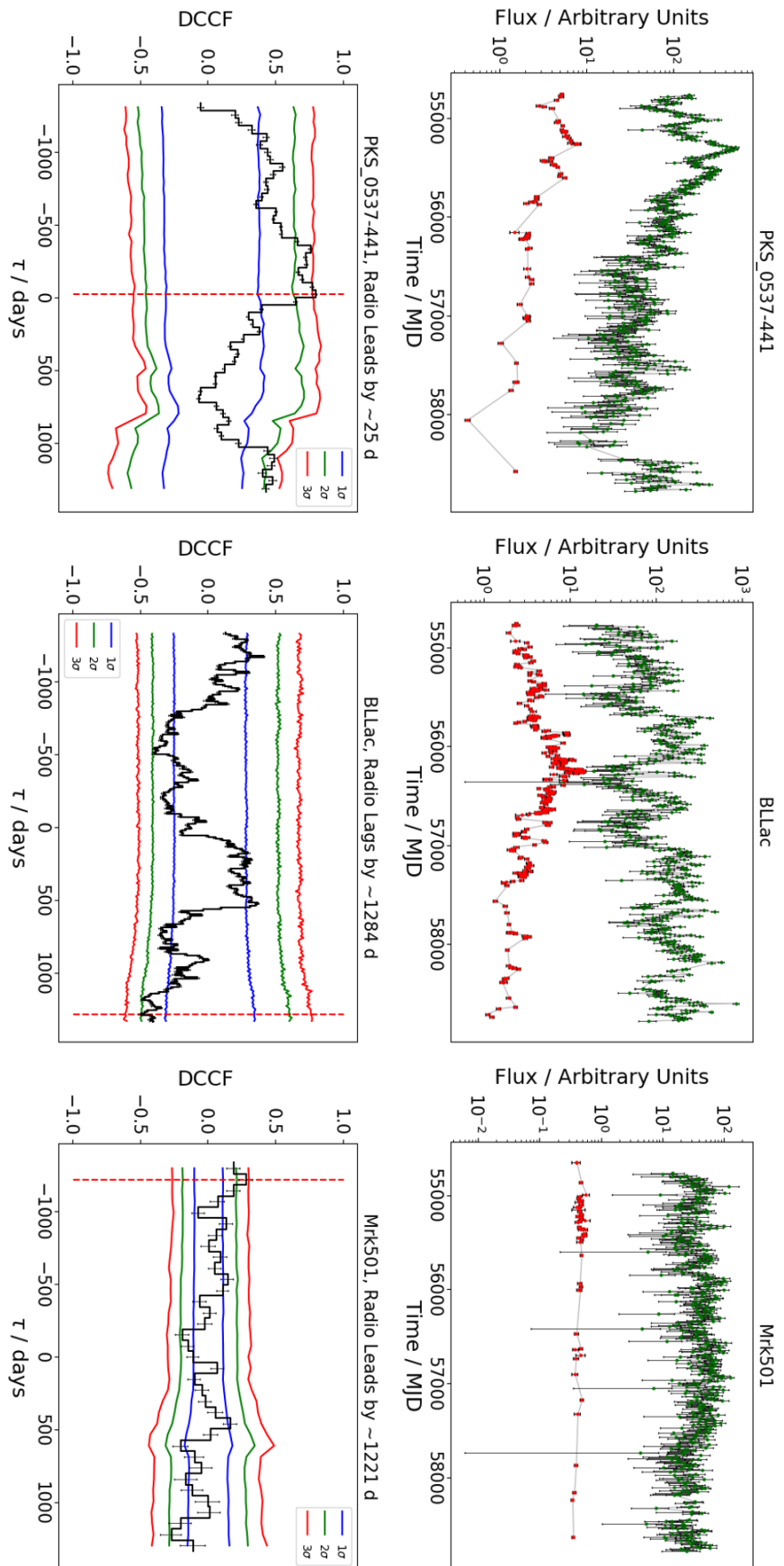
(B6) Mrk 501: DCCF exhibits a single significant positive peak, $2.67^{+1.34}_{-0.49}\sigma$ at -1219 ± 75 d. B6 has the lowest success rates (correlated, $9 \pm 2\%$) and radio sampling (~ 0.11) of all 12 blazars. Contributing LC points ($UCCF < DCCF$) are consistent with the null hypothesis ($\chi^2_\nu = 0.08$). No significant correlation can be claimed, and more radio data is required.

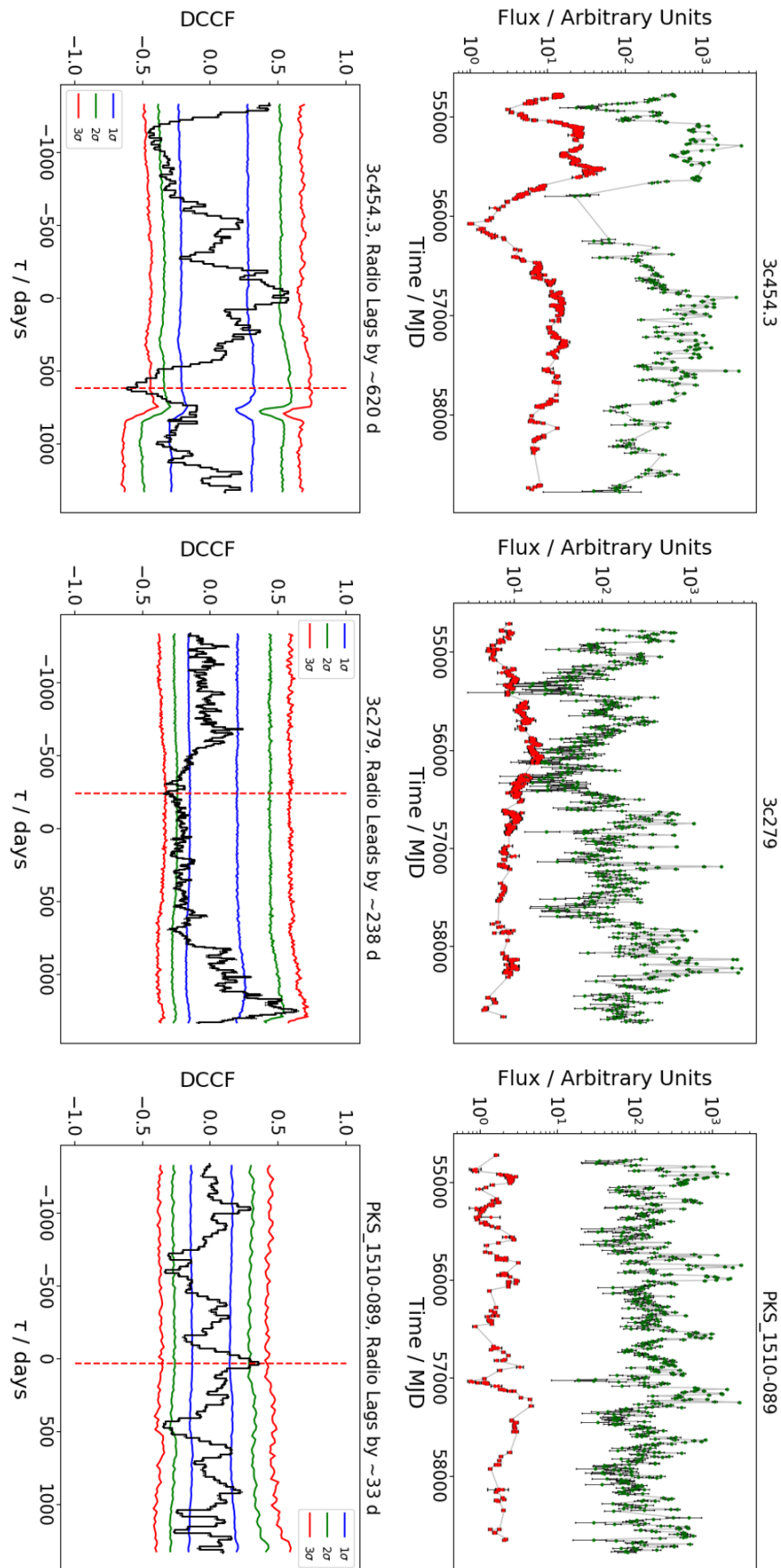
Appendix G TABLES & FIGURES

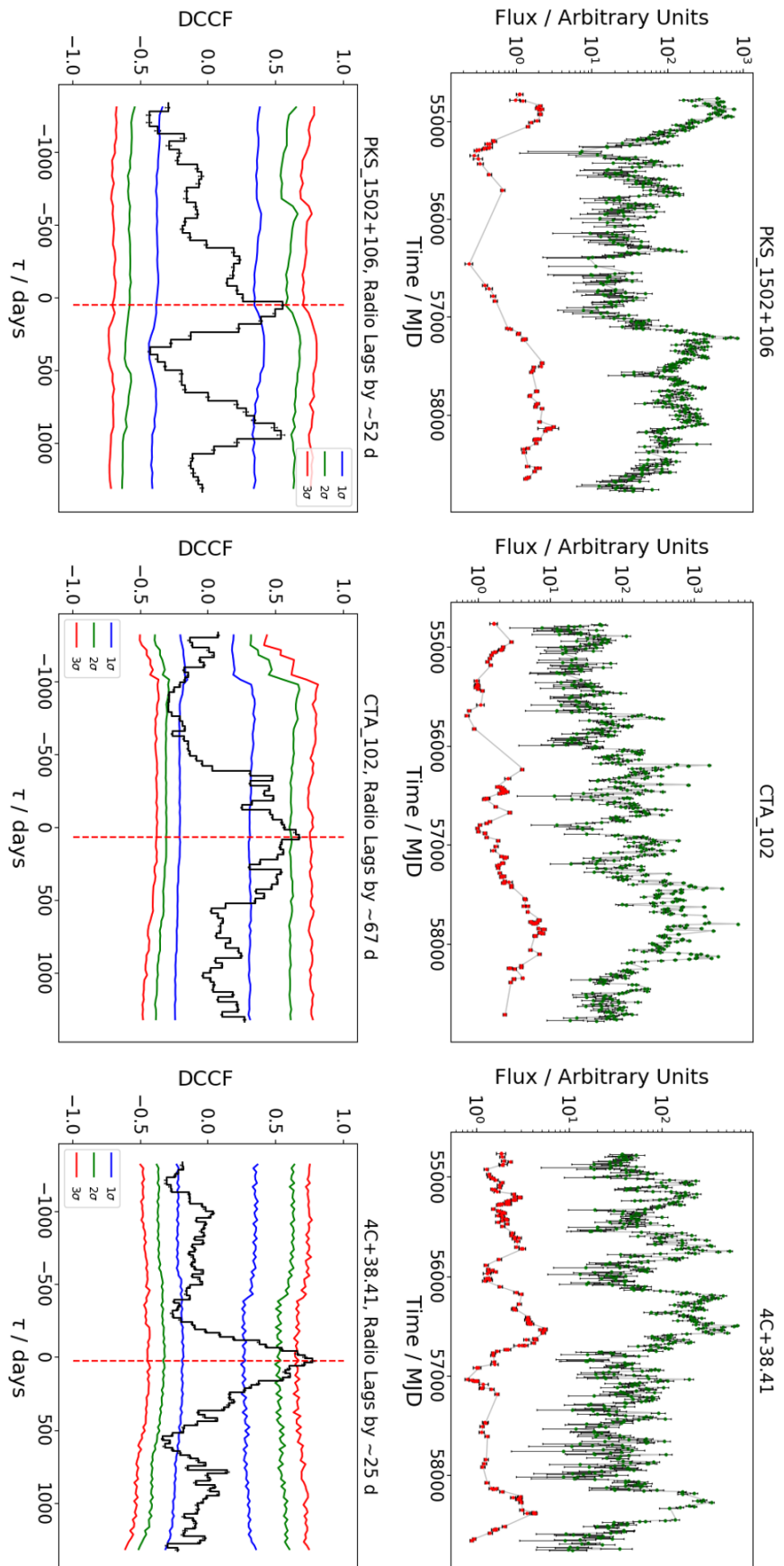
TABLE V: SMA Light Curve data in the 1mm band is taken from the Submillimeter Array Calibrator List at <http://sma1.sma.hawaii.edu/callist/callist.html>. Table details when 1mm observations began ('Data Start'), and the time range that overlaps with our *Fermi*-LAT observations ('Observation Dates', Table. III).

FSRQs	Data Start	Observation Dates	MJD
3C 454.3	11/10/02	26/10/08 - 24/09/19	54765.3 - 58750.2
3C 279	18/02/03	03/09/08 - 20/08/19	54712.1 - 58715.2
PKS 1510-089	03/06/03	13/09/08 - 20/06/19	54722.2 - 58654.2
PKS 1502+106	22/12/04	13/09/08 - 20/06/19	54722.3 - 58654.4
CTA 102	11/10/02	21/10/08 - 13/08/19	54760.2 - 58708.6
4C+38.41	06/11/02	21/10/08 - 20/06/19	54760.2 - 58654.3
<hr/>			
BL Lacs			
Mkn421	15/11/05	03/07/08 - 31/05/19	54650.2 - 58634.2
S5 0716+71	07/11/02	02/10/08 - 13/08/19	54741.4 - 58708.7
PKS 0426-380	09/12/04	18/10/08 - 13/08/19	54757.7 - 58708.6
PKS 0537-441	09/12/04	18/10/08 - 05/04/19	54757.7 - 58578.2
BL Lacertae	11/10/02	14/10/08 - 07/09/19	54753.2 - 58733.5
Mrk501	01/10/04	03/07/08 - 30/05/19	54650.3 - 58633.4

**FIG. 18:** B1 - B3 LCs and Initial DCCFs.

**FIG. 19:** B4 - B6 LCs and Initial DCCFs.

**FIG. 20:** F1 - F3 LCs and Initial DCCFs.

**FIG. 21:** F4 - F6 LCs and Initial DCCFs.